OPEN ACCESS



A Multiwavelength Investigation of PSR J2229+6114 and its Pulsar Wind Nebula in the Radio, X-Ray, and Gamma-Ray Bands

```
I. Pope 1, K. Mori 1, M. Abdelmaguid 2, J. D. Gelfand 2, S. P. Reynolds 3, S. Safi-Harb 4, C. J. Hailey 1, H. An 5, the contraction of the contrac
                                                                                                                                    (NuSTAR Collaboration),
and
P. Bangale<sup>6</sup>, P. Batista<sup>7</sup>, W. Benbow<sup>8</sup>, J. H. Buckley<sup>9</sup>, M. Capasso<sup>10</sup>, J. L. Christiansen<sup>11</sup>, A. J. Chromey<sup>8</sup>, A. Falcone<sup>12</sup>, Q. Feng<sup>8</sup>, J. P. Finley<sup>13</sup>, G. M Foote<sup>6</sup>, G. Gallagher<sup>14</sup>, W. F Hanlon<sup>8</sup>, D. Hanna<sup>15</sup>, O. Hervet<sup>16</sup>, J. Holder<sup>6</sup>, T. B. Humensky<sup>17,18</sup>, W. Jin<sup>19</sup>, P. Kaaret<sup>20</sup>, M. Kertzman<sup>21</sup>, D. Kieda<sup>22</sup>, T. K. Kleiner<sup>7</sup>, N. Korzoun<sup>6</sup>, F. Krennrich<sup>23</sup>, S. Kumar<sup>17</sup>, M. J. Lang<sup>24</sup>, G. Maier<sup>7</sup>, C. E. McGrath<sup>25</sup>, C. L. Mooney<sup>6</sup>, P. Moriarty<sup>24</sup>, R. Mukherjee<sup>10</sup>, S. O'Brien<sup>15</sup>, R. A. Ong<sup>26</sup>, N. Park<sup>27</sup>, S. R. Patel<sup>7</sup>, K. Pfrang<sup>7</sup>, M. Pohl<sup>7,28</sup>, E. Pueschel<sup>7</sup>, J. Quinn<sup>25</sup>, K. Ragan<sup>15</sup>, P. T. Reynolds<sup>29</sup>, E. Roache<sup>8</sup>, I. Sadeh<sup>7</sup>, L. Saha<sup>8</sup>, G. H. Sembroski<sup>13</sup>, D. Tak<sup>7</sup>, J. V. Tucci<sup>30</sup>, A. Weinstein<sup>23</sup>, D. A. Williams<sup>16</sup>, and J. Woo<sup>31</sup>
                                                                                                                                     (VERITAS Collaboration)
                                               <sup>1</sup> Columbia Astrophysics Laboratory, 550 West 120th Street, New York, NY 10027, USA; isaac.pope@columbia.edu
                                                                                               NYU Abu Dhabi, P.O. Box 129188, Abu Dhabi, United Arab Emirates Physics Department, NC State University, Raleigh, NC 27695, USA
                                                                <sup>4</sup> Department of Physics and Astronomy, University of Manitoba, Winnipeg, MB R3T 2N2, Canada
                                                    <sup>5</sup> Chungbuk National University, Chungdae-ro 1, Seowon-Gu, Cheongju, Chungbuk, 28644, Republic of Korea
                                      <sup>6</sup> Department of Physics and Astronomy and the Bartol Research Institute, University of Delaware, Newark, DE 19716, USA
                                                                                                                DESY, Platanenallee 6, D-15738 Zeuthen, Germany
                                                                                   <sup>8</sup> Center for Astrophysics | Harvard & Smithsonian, Cambridge, MA 02138, USA
                                                                                        Department of Physics, Washington University, St. Louis, MO 63130, USA
                                  <sup>10</sup> Department of Physics and Astronomy, Barnard College, Columbia University, NY 10027, USA; capasso@nevis.columbia.edu
                                                                     Physics Department, California Polytechnic State University, San Luis Obispo, CA 94307, USA
                                  <sup>12</sup> Department of Astronomy and Astrophysics, 525 Davey Lab, Pennsylvania State University, University Park, PA 16802, USA
                                                                           Department of Physics and Astronomy, Purdue University, West Lafayette, IN 47907, USA
                                                                                Department of Physics and Astronomy, Ball State University, Muncie, IN 47306, USA
                                                                                             Physics Department, McGill University, Montreal, QC H3A 2T8, Canada
                                      <sup>16</sup> Santa Cruz Institute for Particle Physics and Department of Physics, University of California, Santa Cruz, CA 95064, USA
                                                                                Department of Physics, University of Maryland, College Park, MD 20742-4111, USA <sup>18</sup> NASA GSFC, Greenbelt, MD 20771, USA
                                                                     <sup>19</sup> Department of Physics and Astronomy, University of Alabama, Tuscaloosa, AL 35487, USA
                                                         Department of Physics and Astronomy, University of Iowa, Van Allen Hall, Iowa City, IA 52242, USA
                                                                     Department of Physics and Astronomy, DePauw University, Greencastle, IN 46135-0037, USA
                                                                         Department of Physics and Astronomy, University of Utah, Salt Lake City, UT 84112, USA <sup>23</sup> Department of Physics and Astronomy, Iowa State University, Ames, IA 50011, USA
                                                                <sup>24</sup> School of Natural Sciences, University of Galway, University Road, Galway, H91 TK33, Ireland
                                                                                              School of Physics, University College Dublin, Belfield, Dublin 4, Ireland
                                                                 <sup>26</sup> Department of Physics and Astronomy, University of California, Los Angeles, CA 90095, USA
                     Department of Physics, Engineering Physics & Astronomy, Queen's University, Kingston, ON K7L 3N6, Canada; nahee.park@queensu.ca

28 Institute of Physics and Astronomy, University of Potsdam, 14476 Potsdam-Golm, Germany
                                                     <sup>29</sup> Department of Physical Sciences, Munster Technological University, Bishopstown, Cork, T12 P928, Ireland
                                                        <sup>30</sup> Department of Physics, Indiana University–Purdue University Indianapolis, Indianapolis, IN 46202, USA
                                                31 Columbia Astrophysics Laboratory, 550 West 120th Street, New York, NY 10027, USA; jw3855@columbia.edu
```

Abstract

Received 2022 October 10; revised 2023 October 4; accepted 2023 October 5; published 2023 December 27

G106.3+2.7, commonly considered to be a composite supernova remnant (SNR), is characterized by a boomerang-shaped pulsar wind nebula (PWN) and two distinct ("head" and "tail") regions in the radio band. A discovery of very-high-energy gamma-ray emission ($E_{\gamma} > 100~{\rm GeV}$) followed by the recent detection of ultrahigh-energy gamma-ray emission ($E_{\gamma} > 100~{\rm TeV}$) from the tail region suggests that G106.3+2.7 is a PeVatron candidate. We present a comprehensive multiwavelength study of the Boomerang PWN (100'' around PSR J2229+6114) using archival radio and Chandra data obtained two decades ago, a new NuSTAR X-ray observation from 2020, and upper limits on gamma-ray fluxes obtained by Fermi-LAT and VERITAS observatories. The NuSTAR observation allowed us to detect a 51.67 ms spin period from the pulsar PSR J2229+6114 and the PWN emission characterized by a power-law model with $\Gamma = 1.52 \pm 0.06$ up to 20 keV. Contrary to the previous radio study by Kothes et al., we prefer a much lower PWN *B*-field ($B \sim 3~\mu G$) and larger distance ($d \sim 8~{\rm kpc}$) based on (1) the nonvarying X-ray flux over the last two decades, (2) the energy-dependent X-ray size of the PWN resulting from synchrotron

burn-off, and (3) the multiwavelength spectral energy distribution (SED) data. Our SED model suggests that the PWN is currently re-expanding after being compressed by the SNR reverse shock $\sim \! 1000 \, \mathrm{yr}$ ago. In this case, the head region should be formed by GeV–TeV electrons injected earlier by the pulsar propagating into the low-density environment.

Unified Astronomy Thesaurus concepts: Pulsar wind nebulae (2215); X-ray astronomy (1810); Gamma-ray astronomy (628)

1. Introduction

Pulsar wind nebulae (PWNe; Cholis et al. 2018) are believed to generate a majority of the energetic leptons in our Galaxy. The pulsar's rotating magnetic fields produce a wind of highly relativistic particles that expand out into the shell of the supernova remnant (SNR). High-energy observations of dozens of PWNe detected synchrotron and inverse-Compton upscattering (ICS) of cosmic microwave background photons, ambient infrared (IR), or optical stellar radiation in the X-ray and TeV bands, respectively, suggesting that nonthermal particles are accelerated to TeV or even PeV energies within the PWNe (Arons 2012). The evolution of PWNe is characterized by three stages: (1) young, termination-shockdriven wind nebulae, (2) middle-aged PWNe interacting with their host SNRs, and (3) relic PWNe (Gaensler & Slane 2006; Giacinti et al. 2020). Relativistic winds from the pulsar injected into the center of the SNR are abruptly decelerated in an inward-facing termination shock, at which particles are accelerated to TeV energies; the postshock flow further decelerates until it reaches pressure equilibrium with the SNR interior. The bubble of shocked pulsar wind is the observed PWN, which continues to expand until the deceleration of the outer SNR blast wave sends a reverse shock back toward the center, compressing and rebrightening the PWN, at an age of the order of 1–10 kyr. The PWN continues to interact with the SNR interior until either the SNR dissipates or the pulsar, if born with a substantial kick velocity, escapes the SNR shell and continues to inflate a PWN. In either case the PWN now interacts directly with the interstellar medium (ISM; a "relic PWN"; Cholis et al. 2018), often in the shape of a bow-shock nebula. These middle-aged PWNe manifest a vast diversity of highly anisotropic nonthermal emission in multiple wavelength bands. The composite system is formed by its relic PWN interacting with the ambient medium and SNR reverse shock, and exhibiting peculiar radio and X-ray morphology (often with nicknames such as Rabbit and Snail). Composite SNRs are of particular interest because they manifest sites of on-going PWN-SNR interaction and possibly accelerate particles to TeV-PeV energies (Ohira et al. 2018). Some of the middleaged PWNe are associated with the PeVatron candidates detected by HAWC and LHAASO above $E_{\gamma} \sim 100$ TeV (Abeysekara et al. 2020; Cao et al. 2021). Eventually, after $\tau \sim 100$ kyr, electrons and positrons escape from relic PWNe and form extended TeV halos, as revealed around the Geminga and Monogem pulsars (Abeysekara et al. 2017). TeV halos are a new class of gamma-ray sources and are suggested to be the primary source of the positron excess observed at Earth (López-Coto et al. 2022). How and when a PWN evolves through these transitions depends on the progenitor star's characteristic properties and environment within the ISM. Hence, multiwavelength observations of PWNe in different evolutionary stages and environments are essential for understanding how particles are injected from the pulsar, diffuse out while cooling, and interact with the ambient gas and their host SNRs.

The Boomerang region is one of the most remarkable composite SNRs for its complex multiwavelength morphology and the recent detection of gamma rays above 100 TeV that indicates it to be a PeVatron candidate. Its large-scale radio emission (G106.3+2.7) consists of a compact boomerangshaped nebula around the radio pulsar PSR J2229+6114 and cometary structure extending toward the southwest. The radio source G106.3+2.7 was first identified as an SNR by Joncas & Higgs (1990) following the Dominion Radio Astrophysical Observatory (DRAO) survey of the northern Galactic plane. Using further DRAO observations in the 408 MHz and 1420 MHz continuum bands, Pineault & Joncas (2000) discerned two distinct regions of SNR G106.3+2.7, labeled the head and the tail (see Figure 1). The head region is characterized by its higher surface brightness and flatter spectral index than the elongated tail region. Using Very Large Array (VLA) observations at 20 and 6 cm, as well as ROSAT and ASCA observations, Halpern et al. (2001b) identified a compact radio and X-ray source in the northeast area of the head region of SNR G106.3+2.7 and suspected it to be a pulsar with a corresponding PWN. The radio and X-ray detections of a 51.6 ms pulsation from the pulsar, now known as PSR J2229+6114, confirmed this hypothesis (Halpern et al. 2001a). Further radio and X-ray timing studies of the pulsar led to the determination of a spin-down power of 2.2×10^{37} erg s⁻¹ and a characteristic age of \sim 10 kyr (Halpern et al. 2001a). A compact PWN with an $r \sim 100''$ extent was detected in the radio band and was suggested to be associated with SNR G106.3+2.7 based on the subsequent measurement of the same peak H I velocity from the compact Boomerang nebula and the head region (Kothes et al. 2001). While SNR G106.3+2.7 has been labeled as an SNR, no thermal X-ray emission is reported anywhere in the Boomerang complex, and no large-scale radio morphological features are evident that might suggest the supernova blast wave. The larger-scale integrated radio spectral index is -0.61(Kothes et al. 2006), while that of the PWN alone is ~ 0 (Halpern et al. 2001a), suggesting a shock acceleration source for the larger-scale electrons, but there is no edge brightening apparent at any location.

It has been hypothesized that the Boomerang's shape could be caused by a bow shock between PSR J2229+6114 and its surrounding medium. However, this was deemed unlikely, as simple modeling of the system under this assumption resulted in a supernova explosion energy far below anything ever recorded; the pulsar also does not lie at the apex of the bow structure (Kothes et al. 2001, 2006). In contrast, based on the boomerang-like radio morphology as well as its proximity to the northeast boundary of SNR G106.3+2.7, it was postulated that the PWN had been crushed by an SNR reverse shock (Kothes et al. 2001, 2006). Further observations of the Boomerang region with the Effelsberg 100 m telescope led to a hypothesis that an interaction with the SNR reverse shock

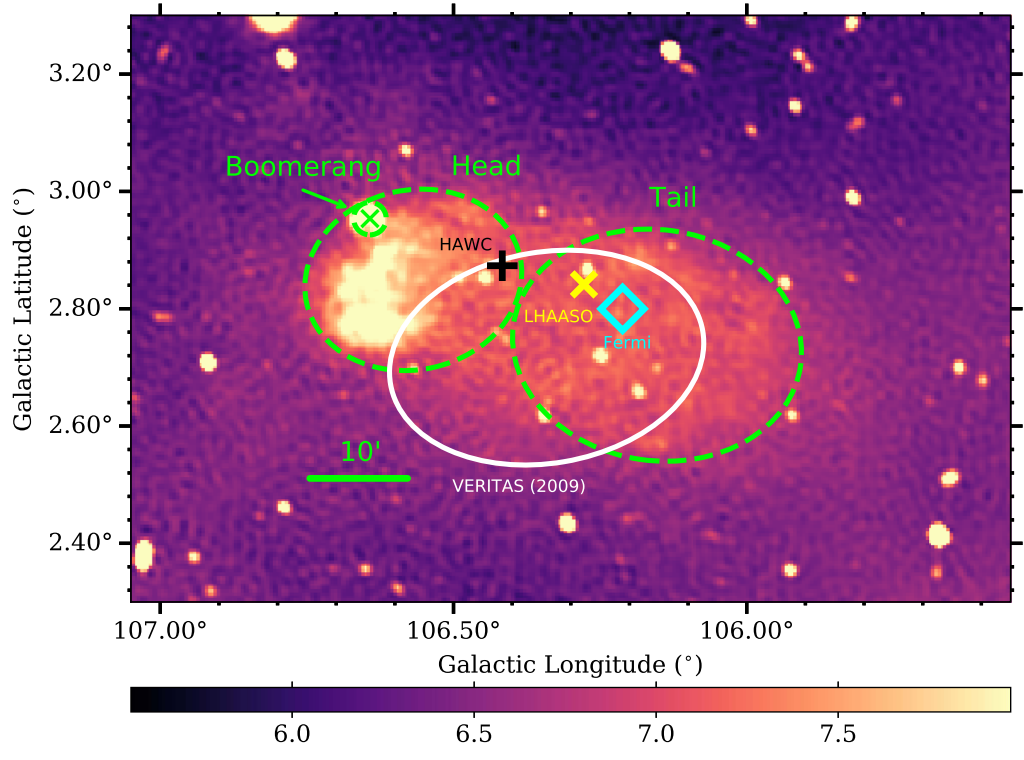


Figure 1. CGPS map of 1420 MHz radio temperature brightness [K] of the SNR G106.3+2.7 region with the head, tail, and PWN indicated by green dashed lines. The pulsar location is marked by the green cross. The white ellipse represents the extent of the gamma-ray emission previously detected by VERITAS. The black plus, yellow cross, and cyan diamond represent the centroids of the gamma-ray emission detected by HAWC, LHASSO, and Fermi-LAT, respectively.

could also account for the low radio luminosity of the PWN with respect to the spin-down power (Kothes et al. 2006). Furthermore, a radio spectral break observed between 4 and 5 GHz was attributed to synchrotron cooling. Under this assumption, Kothes et al. (2006) suggested that the PWN *B*-field is 2.6 mG and that the PWN was crushed by the SNR reverse shock 3900 yr ago. A more recent study based on a model of the diffusion of the relativistic electrons injected into the PWN and X-ray radial profile suggested that the PWN *B*-field is $140 \,\mu$ G (Liang et al. 2022).

In the X-ray band, the pulsar, its compact nebula $(r \sim 30'')$, and diffuse emission over $r \lesssim 100''$ were detected by two Chandra observations (17 and 94 ks) in 2001–2002 (Halpern et al. 2001a). XMM-Newton and Suzaku observations revealed more extended diffuse X-ray emission from the head and tail regions (Fujita et al. 2021; Ge et al. 2021). The long Chandra observation in 2002 unveiled a point source at the pulsar position, an incomplete torus of $r \sim 10''$, and a jet-like feature. These X-ray features resemble those of the Vela PWN, whose pulsar's motion is aligned with its X-ray jet (Halpern et al. 2002). The Chandra ACIS image of the Boomerang PWN was fit by a 3D torus model (Ng & Romani 2004). The brighter side of the torus (west; see Figure 3) is due to Doppler boosting of mildly relativistic magnetohydrodynamic outflow from the termination shock. The best-fit torus model predicts that the pulsar should be moving along the spin axis (i.e., the jet direction toward the northwest). The prediction that the pulsar is moving toward the northwest does not seem to agree with the tail morphology of SNR G106.3+2.7. However, the recent numerical studies studying the evolution of a PWN while interacting with a host SNR show that the PWN's morphology depends on both the pulsar's proper motion and the region's density gradient (Kolb et al. 2017).

Gamma-ray emission has been observed in the region of SNR G106.3+2.7 from the GeV energy range up to a few hundred TeV. The Large Area Telescope on board the Fermi gamma-ray space telescope (Fermi-LAT) detected GeV emission coincident with PSR J2229+6114, which was also associated with EGRET source 3EG J2227+6122 (Hartman et al. 1999; Abdo et al. 2009b). Gamma-ray pulsations were observed above 0.1 GeV, confirming GeV emission originates from PSR J2229+6114 (Abdo et al. 2009a). Using a collection of Fermi-LAT data, Xin et al. (2019) identified emission between 3 and 500 GeV coincident with the tail region with a source radius 0°25. The Very Energetic Radiation Imaging Telescope Array System (VERITAS) detected TeV emission from the tail region and found that the centroid of the TeV source overlaps with 12 CO cloud J = 1-0 emission (Acciari et al. 2009). More recently, the MAGIC collaboration reported TeV detection of the head region as well (Oka et al. 2021). Emission of gamma rays with energies higher than 100 TeV was detected by HAWC (Albert et al. 2020), Tibet AS γ (Amenomori et al. 2021), and LHAASO (Cao et al. 2021); the ultrahigh-energy (UHE) source is coincident with the VER-ITAS and Fermi-LAT sources in the tail region as well as with PSR J2229+6114 (Albert et al. 2020). The UHE detection identified the Boomerang region as a PeVatron candidate, but its origin is still debated between the leptonic and hadronic cases associated with the Boomerang PWN and the SNR interaction with molecular clouds, respectively (Bao & Chen 2021; Fujita et al. 2021; Ge et al. 2021; Breuhaus et al. 2022; Liu et al. 2022). Various high-energy emission centroids/extents are depicted over the map of 1420 MHz radio temperature brightness of SNR G106.3+2.7 in Figure 1.

The distance to the Boomerang complex is unusually poorly determined, even among supernova remnants. A list of the

Table 1
Boomerang Distance Estimates

d	Method	Citation
0.8 kpc	H I radial velocities	Kothes et al. (2001)
3 kpc	Column density $(N_{\rm H})$	Halpern et al. (2001b)
5–7.5 kpc	Dispersion measurement	Abdo et al. (2009a), Yao et al. (2017)
12 kpc	H I radial velocities	Pineault & Joncas (2000)

various distance measurements is provided in Table 1. Pineault & Joncas (2000) reported radio continuum observations with DRAO at 408 and 1420 MHz, as well as H I observations, in which they identified an absorption feature at -104 km s⁻¹, giving a kinematic distance of 12 kpc. This would put G106.6 +2.9 at a z-height of 607 pc above the Galactic plane, with a linear extent of over 200 pc. However, Halpern et al. (2001b) suggested a much closer distance based on the measurement of an absorbing column density. They observed the PWN region with radio (VLA) and X-ray (ASCA) telescopes in order to search for a counterpart of the unidentified EGRET gamma-ray source 3EG J2227+6122. In this study, they obtained an absorbing column $N_{\rm H}$ of 6.3×10^{21} cm⁻². Since the column density through the entire Galaxy is only $8.4 \times 10^{21} \, \text{cm}^{-3}$ in that direction, they concluded that the PWN was at least 2 kpc away, perhaps much further, and assumed a fiducial distance of 3 kpc. The pulsar discovery Halpern et al. (2001a) reported a dispersion measure (DM) of $200 \pm 10 \text{ cm}^{-3}$ pc, which, with the Taylor & Cordes (1993; TC93) electron-density model, implies a distance of 12 kpc (Taylor & Cordes 1993). A revised n_e model, NE2001 (Cordes & Lazio 2002), gives 7.5 kpc for the same DM value (Abdo et al. 2009a). Yao et al. (2017) proposed a new $n_{\rm e}$ model (YMW16) to estimate the distance to the pulsars using the same DM value. YMW16 estimated the distance to the Boomerang PWN to be 5.037 kpc with an error of 40 %. This error is larger than 20 %, the threshold YMW16 considered for their model estimation to be satisfactory. Yao et al. (2017) also note that the distance to the Boomerang PWN showed the largest impact due to the Galactic warp. A distance of 3 kpc would imply, from TC93, a DM of only 75 cm⁻³ pc (Halpern et al. 2001a). Kothes et al. (2001) suggested a very near distance, 800 pc, based on morphological correspondences between the radio continuum image and channel maps of HI and CO from surveys, at velocities of about -6 km s^{-1} . Kothes et al. (2004) presented a new technique of HI absorption of polarized emission for distance determinations; they pointed to the absence of an absorption feature in the range from -70 to -55 km s⁻¹, which they asserted would be present if G106.6 +2.9 were further away than the Perseus arm at about 3 kpc.

The ambiguity in the distance of G106.6+2.9 may be rooted in its relatively high Galactic latitude of 2°.9. Over 85% of the 383 Galactic SNRs in the catalog of Ferrand & Safi-Harb (2012) are closer to the Galactic plane than this. At 3 kpc, for instance, G106.6+2.9 has a *z*-height of 150 pc, higher than the H I scale height of the Galactic disk of about 100 pc, and perhaps explaining anomalous H I absorption (or its absence).

The properties of G106.6+2.9 are extreme at either distance: 0.8 kpc or 12 kpc. At 0.8 kpc, as pointed out by Kothes et al. (2006), the PWN would have an extremely low ratio of radio luminosity to pulsar \dot{E} . Additionally, the H I column density from X-ray observations of 6.3×10^{21} cm⁻² implies a mean volume density of neutral atomic H of 2.6 cm⁻³ between Earth

and G106.6+2.9, which is unrealistically high. At 12 kpc, Halpern et al. (2001a) state that the pulsar would need to be more efficient than the Crab or Vela pulsars at converting spindown luminosity into >100 MeV gamma rays.

In this paper, we present a multiwavelength analysis of the Boomerang PWN region. We shall refer to the compact radio and X-ray source within 100" of the pulsar as the PWN, and as distinct from the head (scale $\sim 15'$) and tail (scale $\sim 30'$) regions. Our work is focused on this PWN region, in contrast to the recent publication by Fang et al. (2022) for example, which primarily concerns the larger-scale nebula. Our motivation is to better constrain the characteristic properties and gain further insight into the formation of the Boomerang PWN. In doing so, we gain a better understanding of the Boomerang PWN's relationship to the high-energy emission coincident with SNR G106.3+2.7, which is mostly confined to the SNR's tail region. We begin by describing the archival Chandra and new NuSTAR X-ray observations and our timing, imaging, and spectral analysis (Section 2.1). In Sections 2.2 and 2.3 we describe the gamma-ray observations of the Boomerang PWN region and analysis of the corresponding data from Fermi-LAT and VERITAS, respectively. We then combine the multiwavelength spectral data of the Boomerang PWN and explore various models that could describe the PWN's emission through fitting of the spectral energy distribution (SED, Section 3). For the SED models, we consider the two most extreme source distances, 0.8 and 7.5 kpc, from Table 1. (From the two distance measurements based on HI radial velocity measurements, we chose 0.8 kpc over 12 kpc as it is the more recent estimation.) In the end, we determine the source distance from the SED and from analysis of the X-ray morphology of the Boomerang PWN region, within 100" of the pulsar. We do not consider the emission on larger scales. Finally, we discuss the results from our X-ray and multiwavelength analysis and constrain the PWN B-field (Section 4). We contemplate the current evolutionary phase of the Boomerang PWN and examine its relation to the high-energy emission coincident with SNR G106.3+2.7. We summarize our results in Section 5.

2. Observations and Data Analysis

We present X-ray, GeV (Fermi-LAT), and TeV (VERITAS) gamma-ray observations of the Boomerang PWN in the following sections. We performed X-ray analysis of the 2002 Chandra and 2020 NuSTAR observation data (Section 2.1). Fermi-LAT and VERITAS data analysis was confined to only the Boomerang PWN region, and the source extraction region varied according to the point-spread function (PSF) of each telescope (Sections 2.2 and 2.3). All errors are given to the 2σ confidence level unless explicitly stated otherwise.

2.1. X-Ray Observations

Chandra observed the Boomerang region with its CCD ACIS-I array on 2002 March 15 (ObsID 2787, PI Halpern) for ~94 ks of exposure. The observation files were processed and analyzed using the tools in CIAO v4.13. NuSTAR observed PSR J2229+6114 and its PWN on 2020 September 21 (ObsID 40660001002) for a total exposure of 45 ks. Data analysis was conducted using the NuSTARDAS v2.0.0 subpackage within HEASOFT v6.28. CIAO v4.13 was also used for its image modeling and fitting application (SHERPA).

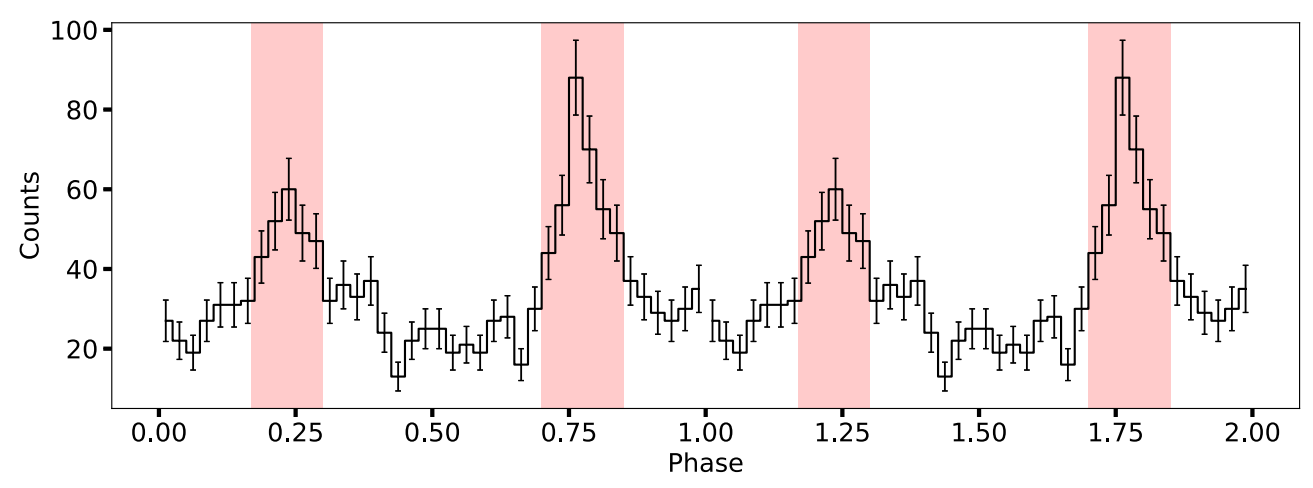


Figure 2. NuSTAR 3–20 keV folded light curve of PSR J2229+6114. The pulsed phase ranges excised from our PWN imaging and spectral analysis are demarcated by the red regions.

The Boomerang PWN region is composed of four components: (1) the pulsar (PSR J2229+6114), (2) a torusjet feature, which represents the termination shock region $(r \sim 10'')$; Ng & Romani 2004), (3) the X-ray PWN $(r \sim 30'')$, and (4) diffuse X-ray emission ($r \sim 100''$). These X-ray features are resolved by Chandra as shown in the Chandra image in the 0.5–8.0 keV band (Figure 3); the radial profile for the Chandra image is shown in Figure 4. Since NuSTAR (with 58" halfpower diameter) cannot spatially resolve the pulsar from the extended X-ray emission, we first performed timing analysis on the NuSTAR data in order to remove the pulsar emission (Section 2.1.1). We then present NuSTAR imaging analysis in different energy bands in comparison with the high-resolution Chandra images below 8 keV (Section 2.1.2). In Section 2.1.3, we analyze X-ray spectral data of the PWN by excising the pulsar emission spatially (for Chandra) and by selecting a phase interval for the off-pulse component (for NuSTAR).

2.1.1. NuSTAR Timing Analysis

We found that X-ray emission from the Boomerang pulsar + nebula system was detected up to 20 keV. We limited our timing analysis to the 3–20 keV band. The NuSTAR telescope consists of two focal plane modules (FPMA and FPMB), which are described in detail in Harrison et al. (2013). We determined the source centroid for both FPMA and FPMB images using DS9's centroid function. We then applied barycentric correction to the event files using barycorr, and extracted source events from an r = 30'' circular region around the source centroid. Using the Stingray X-ray timing analysis package (Bachetti et al. 2022), we applied the Z^2 algorithm with two harmonics in order to search the combined event times from both focal plane modules for pulsations. A strong periodic signal with $P = 51.671495^{+1}_{-3} \times {}^{10^{-6}}_{10^{-6}}$ ms $(3\sigma \text{ error bars})$ was detected with $Z_2^2 = 174$. This period differs slightly from that reported by Halpern et al. (2001a) after accounting for the \dot{P} quoted in the same paper, P = 51.67199357(0), indicating an undetected timing glitch. Folding upon the measured period, we generated a pulse profile in the 3–20 keV band (Figure 2). The on-pulse component is clearly identified as an asymmetric double peak in the folded light curve, consistent with the pulse profiles measured by Halpern et al. (2001a) and Kuiper & Hermsen (2015). We considered our baseline off-pulse component to be around 25-30 counts per bin. As a

conservative estimate for the pulsed emission, we only excised the clear peaks significantly above the baseline. After calculating a phase value for each photon event, we removed the on-pulse events between $\phi=0.17$ and 0.30, as well as between $\phi=0.70$ and 0.85 using extractor for subsequent spectral and imaging analysis of the nebular emission. The effect of any leftover pulsar component after phase extraction is negligible, as we determine in Section 2.1.3.

2.1.2. NuSTAR and Chandra Imaging Analysis

The Chandra observations detected the Boomerang PWN extending to the bounds of its radio emission ($r \approx 100''$; Halpern et al. 2001a). We thus considered r = 100'' as the outermost boundary of the X-ray nebula for NuSTAR imaging analysis using the phase-resolved event files after excising the pulsed emission. The broad bandwidth of NuSTAR allows us to compare the X-ray image of Boomerang in different energy ranges. We performed energy-resolved imaging analysis in a "soft" band (3–10 keV) and a "hard" band (10–20 keV). For each of the FPMA and FPMB data, we corrected the positional offsets between the NuSTAR source centroid (measured in the on-pulse images) and the pulsar position measured by Chandra.

The event files for both FPMA and FPMB were split into the soft and hard bands with extractor. Exposure maps were created with nuexpomap for each event file with vignetting effects at 6.5 and 15 keV for the soft and hard bands, respectively. The FPMA and FPMB event files were combined for each energy band, and the same was done for the exposure maps. For the purpose of smoothing out spurious features near the detector edges, the summed NuSTAR images were convolved with a Gaussian kernel of $\sigma = 2.46$ (corresponding to the NuSTAR pixel size) before being divided by the corresponding exposure maps (Nynka et al. 2014). The above process produced an exposure-corrected mosaic flux image for each energy band. In each energy band, we calculated the background level using a region to the northeast of Boomerang, avoiding the diffuse X-ray emission detected by Ge et al. (2021). The resultant 3-10 keV and 10-20 keV backgroundsubtracted flux images of the Boomerang PWN are shown in Figure 5.

In order to characterize the Boomerang PWN emission, we compared radial profiles around the pulsar position in the two

energy bands, as well as the NuSTAR PSF for determining a source extent. A set of 20 annuli between $r_{\rm in}=5''$ and $r_{\rm out}=100''$ were centered on the source centroid of the mosaic image. The radial profiles for each energy band were extracted from these annuli and normalized so that the brightness was set to 1 at r=0. The same set of annuli was used to create a normalized radial profile of the NuSTAR 8–12 keV PSF to serve as a point-source template. Since we found that the NuSTAR PSF varies insignificantly in 3–20 keV, we chose 8–12 keV to produce the radial profile representative of our case. The soft, hard, and PSF radial profiles are shown in Figure 6.

The background-subtracted source profiles, as shown in Figure 6, are extended above the NuSTAR PSF up to $r \sim 100''$. The radial profiles in both the soft and hard bands appear more extended than the NuSTAR PSF profile. Furthermore, the soft band exhibits a slightly wider radial profile than that of the hard band. To determine the size of the nebula in each energy band more quantitatively, we fit the NuSTAR images using SHERPA. We modeled the X-ray source as a 2D Gaussian and included a constant background level. The source model was convolved with the NuSTAR PSF and then fit to the NuSTAR image data. After taking into account the telescope dithering, we produced the effective NuSTAR PSF data in 4.5-6 keV and 12-20 keV for the soft and hard bands, respectively (Nynka et al. 2014). The fit yielded an FWHM of $33'' \pm 2''$ for the soft band and $20'' \pm 2''$ for the hard band; the errors represent the 1σ confidence intervals (see Figure 6).

For the purpose of illustrating the various regions of interest in the Boomerang PWN and comparing with the NuSTAR images, we created a high-resolution radial profile of the Chandra 0.5–8 keV image shown in Figure 4. To produce this radial profile, we generated a set of 20 annuli around the pulsar position from $r_{in} = 1''$ (to mask out the pulsar emission) to $r_{\text{out}} = 100''$ (i.e., the boundary of the X-ray nebular emission). The profile produced from these annuli was normalized, and the background surface brightness was extracted from the same region used for extracting background spectra. The radius of the diffuse X-ray extent measured by Halpern et al. (2001a) and the NuSTAR 3-10 and 10-20 keV PWN radii are plotted over the resulting radial profile in Figure 4. The FWHM of the soft and hard X-ray emission detected by NuSTAR (r = 33'' and 20") corresponds to the inner PWN where most of the X-ray nebular emission is concentrated.

2.1.3. Chandra and NuSTAR Spectral Analysis

In this section, we present our Chandra and NuSTAR spectral analysis of the entire PWN region from r = 100''. This region is in accordance with the Boomerang radio PWN, thus it is appropriate for subsequent SED studies (e.g., Section 3.1). Using the CIAO specextract script, the Chandra spectrum was extracted from the r = 100'' circular region around the pulsar position, excluding the pulsar emission in r < 1''. Increasing the exclusion region to r < 3'' had no significant effect on our spectral fits, suggesting that r < 1'' is sufficient for excising the pulsed emission component. A source-free region to the immediate northwest of the source extraction region was used for extracting background spectra. In contrast to the Chandra spectral analysis, we performed NuSTAR spectral analysis on the off-pulse events of the Boomerang region. We used an r = 100'' circular source region around the emission centroid (which was previously adjusted to the pulsar position in the data from each module). The NuSTAR response matrix and effective area files were created using nuproducts for an extended source option. We used two different approaches to produce NuSTAR background spectra: by modeling the background using nuskybkg (Wik et al. 2014) and by extraction from an off-source region with nuproducts. In the former method, we modeled background spectra with nuskybkg by fitting actual background spectra extracted from multiple source-free regions across the NuSTAR detector chips for both modules. In the latter method, a source-free region on the same detector chip as the source was used for generating background spectra. In both cases, background regions were selected to avoid the additional diffuse nonthermal X-ray emission in the head region (Ge et al. 2021). We found that fitting the source spectra with the background spectra produced by either method yielded statistically identical results. Hereafter we present our NuSTAR spectral analysis results with the standard background extraction using nuproducts.

The NuSTAR and Chandra spectra were adaptively binned to 2.5σ and 2.0σ over background counts, respectively. In order to determine the hydrogen column density accurately, we fit the 0.5–8.0 keV Chandra spectrum with an absorbed power-law model in XSPEC v12.12.0. The fit was first carried out using the default abundance data (Anders & Grevesse 1989), resulting in the best-fit column density $N_{\rm H}=6.2^{+1.0}_{-0.9}\times10^{21}~{\rm cm}^{-2}$. We then repeated the Chandra spectral fit using the Wilms abundance table (Wilms et al. 2000), obtaining a higher value of $N_{\rm H}=8.9^{+1.5}_{-1.4}\times10^{21}~{\rm cm}^{-2}$. Radio observations of PSR J2229+6114 measured its DM to be $(204.97\pm0.02)~{\rm cm}^{-3}$ pc (Abdo et al. 2009a). Using a linear relation between $N_{\rm H}$ and DM as well as its slope errors (He et al. 2013), we derived $N_{\rm H}=(4.3-8.8)\times10^{21}~{\rm cm}^{-2}$. The hydrogen column densities obtained by the Chandra observation and estimated from the DM measurement are consistent with each other.

We proceeded with spectral fitting using this updated $N_{\rm H}$ value found using the Wilms abundance table. The NuSTAR FPMA and FPMB 3-20 keV spectra were jointly fit using an absorbed power-law model with independently varying FPMA and FPMB flux normalization variables, with the hydrogen column density fixed to $N_{\rm H}=8.9\times10^{21}~{\rm cm}^{-2}$. This allowed us to find the ratio between the FPMA and FPMB flux normalization values (i.e., the cross-normalization factor). We also created a joint fit using the Chandra 0.5–8.0 keV and NuSTAR 3–20 keV spectra, again with an absorbed power-law model. In this case, FPMA and FPMB were forced to share a flux normalization value, independent of Chandra's. The resulting joint fit measured the photon index to be $\Gamma=1.52\pm0.06$ with a reduced chi-squared value of $\chi^2_{\nu}=0.95$ (226 degrees of freedom, or dof), consistent with the photon indices of the individual NuSTAR and Chandra spectral fits within error (see Table 2). A broken power law or an additional spectral component was not statistically required given the goodness of fit with a single power-law model. The NuSTAR spectra and NuSTAR-Chandra joint spectra with the best-fit models are presented in Figure 7. The parameters from these fits, as well as from the Chandra spectral fit, are listed in Table 2. Given that the cross-normalization factor for the joint fit ($C = 0.92^{+0.09}_{-0.08}$) is consistent with 1, no significant change in X-ray flux was detected from the PWN between the 2002 Chandra and 2020 NuSTAR observations.

In order to confirm that our NuSTAR PWN spectrum was not significantly tainted by pulsar emission after phase

 Table 2

 Boomerang PWN Spectral Fitting Parameters

Parameter	NuSTAR	NuSTAR + Chandra	Chandra Chandra	
Model	tbabs*const*pow	tbabs*const*pow	tbabs*pow	
$N_{\rm H} [10^{22} {\rm cm}^{-2}]$	0.89 (frozen)	0.89 (frozen)	$0.89^{+0.15}_{-0.14}$	
$\Gamma_{\mathbf{X}}$	1.52 ± 0.15	1.52 ± 0.06	$1.52^{+0.13}_{-0.12}$	
Flux normalization ^a	$1.89^{+0.63}_{-0.49}$	1.95 ± 0.11	$1.94^{+0.33}_{-0.28}$	
Cross-normalization	$0.85^{+0.11}_{-0.10}$	$0.92^{+0.09}_{-0.08}$		
χ^2_{ν} (dof)	1.21 (79)	0.95 (226)	0.79 (141)	
$F_{\rm X} (0.5-10 {\rm \ keV})^{\rm b}$	0.98 ± 0.06	1.10 ± 0.03	1.15 ± 0.04	
$F_{\rm X} (10-20 {\rm \ keV})^{\rm b}$	0.70 ± 0.04		•••	

Notes. All errors are given to the 90% confidence level.

Absorbed X-ray flux in units of 10^{-12} erg s⁻¹ cm⁻².

extraction, we attempted to characterize the off-pulse pulsar emission. While this was difficult because of the low number of pulsed photon counts, we decided upon the following method. In order to characterize the on-pulse pulsar component, we extracted the on-pulse NuSTAR 3-20 keV spectrum from the r = 30'' region around the pulsar position and used the corresponding off-pulse spectrum as background. We then jointly fit this spectrum with the Chandra 2–8 keV point-source spectrum, using a tbabs*(pow+const*pow) model. By setting the constant term to zero for the NuSTAR spectrum, to one for the Chandra spectrum, and allowing the first power law to only fit the NuSTAR spectrum, the latter power law characterized the off-pulse pulsar component. We found that the off-pulse pulsar flux component represents only about 10% of the pulsar emission, and only about 5% of the off-pulse emission. We therefore forgo redoing the above spectral analysis with an offpulse pulsar model component; it is negligible.

2.2. Fermi-LAT Data Selection and Analysis

The Fermi Large Area Telescope is a pair-conversion highenergy gamma-ray telescope that can detect gamma rays in the energy range from 20 MeV to above 1 TeV (Atwood et al. 2009). The presented analysis was performed by means of Fermipy, a Python-based package that allows one to analyze Fermi-LAT data with the Fermi Science Tools (Wood et al. 2017). We used Fermipy version v1.0.1, which is associated to the 2.0.8 version of the Fermi Science Tools.

We selected events with time stamps between MET 239557418 (2008 August 4 15:43:37.000 UTC) and MET 644798253 (2021 June 7 22:37:28.000 UTC), in a 10° wide region around the 4FGL catalog counterpart to PSR J2229 +6114, i.e., 4FGL J2229.0+6114. The analysis was conducted in the energy range 3 GeV–2 TeV.

We used P8R3_SOURCE_V3 instrument response functions and event type 3 (front and back conversion type). We binned the data using a spatial size of 0°.1 and eight energy bins per decade. We modeled all the sources within a box of width 20° that are included in the second release of the 4FGL catalog (4FGL-DR2; Acero et al. 2016), along with the isotropic and Galactic diffuse emission (iso_P8R3_SOURCE_V3_v1 and gll_iem_v07).

We first optimized the model by fitting normalization and spectral shape parameters of each source in the region of interest and calculating their test statistics (TS = $-2 \ln (L_{\text{max},0}/L_{\text{max},1})$ where $L_{\text{max},0}$ and $L_{\text{max},1}$ are the maximum likelihoods for a

model excluding and including the source, respectively³²), by using the gta.optimize function. We then simplified the model by removing sources that have TS below 4 (i.e., with a detection significance below ~2 standard deviations) and number of predicted counts below 1, in order to ease convergence of the fit. Before performing the final fit, we freed sources that have TS above 25 (i.e., with a detection significance of ~ 5 standard deviations or above), within a radius of 5° from the target position of 4FGL J2229.0+6114, as well as the isotropic and Galactic diffuse emission components. We also modeled the emission from the tail region of the Boomerang nebula as described by Xin et al. (2019), with a uniform disk with spatial width 0°.25 centered around (R.A., decl.) = (336.68, 60.88) and a power-law spectrum. Figure 8 shows the SED of 4FGL J2229.0+6114. We used the same spectral model as the one reported in the 4FGL-DR2 catalog (PLSuperExpCutoff2). The SED was extracted using the gta.sed() method, which fits the flux normalization of the source in each energy bin, using a power law with a fixed index of -2. We see no emission above 50 GeV (TS of the spectral points is below a threshold value of 4); the differential upper limit in the energy range 50.7 GeV-2 TeV is 2.91×10^{-7} MeV cm⁻² s⁻¹ at 95% confidence level. As outlined in Abdo et al. (2013), pulsar spectra in the LAT energy range should cut off exponentially around a few GeV; for this reason, we conservatively considered only the measurements above 50 GeV as PWN emission in order to cut most of the pulsed emission from 4FGL J2229.0+6114.

2.3. VERITAS Observation and Analysis

VERITAS is an array of four imaging atmospheric Cherenkov telescopes (IACTs), located near Tucson, Arizona, designed to measure gamma rays of energies from 100 GeV up to >30 TeV. Each telescope has a field of view of 3°.5, and the array can detect a pointlike source with 1% of the Crab PWN flux at 5σ significance within 25 hr. VERITAS has an angular resolution of \sim 0°.1 (Park & VERITAS Collaboration 2015). The VERITAS Collaboration previously reported the detection of gamma-ray emission from the region of SNR G106.3+2.7 within 33.4 hr (Acciari et al. 2009) based on data collected in the 2008 epoch. The TeV emission was observed near the central extended radio emission (see Figure 1) rather than the

^a Flux normalization at 1 keV (10⁻⁴ photons cm⁻² s⁻¹ keV⁻¹). For the NuSTAR and joint spectral fits, the flux normalization corresponds to the FPMA and Chandra spectra, respectively.

³² https://fermi.gsfc.nasa.gov/ssc/data/analysis/documentation/Cicerone/Cicerone_Likelihood/Likelihood_overview.html

Table 3
VERITAS Upper Limits with 99% Confidence Level

E _{threshold} (TeV)	Index	Upper Limits $(10^{-12} \text{ s}^{-1} \text{ cm}^{-2})$
0.38	2.0	1.10
0.38	2.5	1.23
0.35	3.0	1.52
0.79	2.0	0.40
0.72	2.5	0.48
0.72	3.0	0.49

location of the Boomerang PWN. From 2009 to 2010, VERITAS accumulated an additional 22.3 hr with a changed array configuration where one telescope was moved to make the array more symmetric, which improved the sensitivity of the array (Perkins et al. 2009). Combined with the previous data set, we used a total exposure of 57.7 hr for the analysis at the location of the Boomerang PWN. As the extent of the PWN measured in radio and X-ray is smaller than the angular resolution of VERITAS, the analysis was performed with an assumption that the emission is a pointlike source. Standard VERITAS analysis was performed with two independent methods. Two different event selections were used for the analysis: one selection was optimized to search for emission that was 2%-10% of the Crab Nebula strength and one selection was optimized to search for emission weaker than 2% of the Crab Nebula strength. The event selections optimized to search for the weaker emission reject the largest fraction of background events, resulting in a higher energy threshold. No strong gamma-ray emission was detected at the location of the Boomerang PWN. Upper limits at the 99% confidence level for two different energy thresholds were calculated based on the assumption of a power-law spectral energy distribution with a spectral index ranging from 2 to 3. The results are shown in Table 3. These upper limits are shown in Figure 9 together with the SED of known very-high-energy (VHE) gamma-ray emission in the tail region of SNR G106.3+2.7.

3. Broadband Spectral Energy Distribution

In this section, we model the multiwavelength data from the radio to the TeV band. We present analyses using three different leptonic SED models, all one-zone (homogeneous) models with varying degrees of spectral detail. As there was no detection of gamma-ray emission above 3 GeV from the Boomerang PWN, we will not consider the effect of adding hadronic components to the model in this paper. We will include hadronic components in a future paper reviewing the SEDs from the entire SNR. The morphological complexity of the Boomerang PWN and larger-scale system is such that all three models used in this paper are highly simplified. And as can be seen in Figures 3 and 5, the X-ray centroid in both the soft and hard bands is offset from the peak in the radio band, suggesting the possibility that Boomerang is a multizone system. By using these one-zone models we assume that both the X-ray and radio emission originate from the same source and physical processes as part of a single system. This assumption has been made for other PWNe with similar offsets between X-ray and radio peak emission, such as the PWNe associated with SNRs G54.1+0.3, G327.1+1.1, and MSH 15 -56 (Lang et al. 2010; Temim et al. 2013, 2015). Despite the simplification made in using these aforementioned models, we hope to obtain general constraints on important parameters,

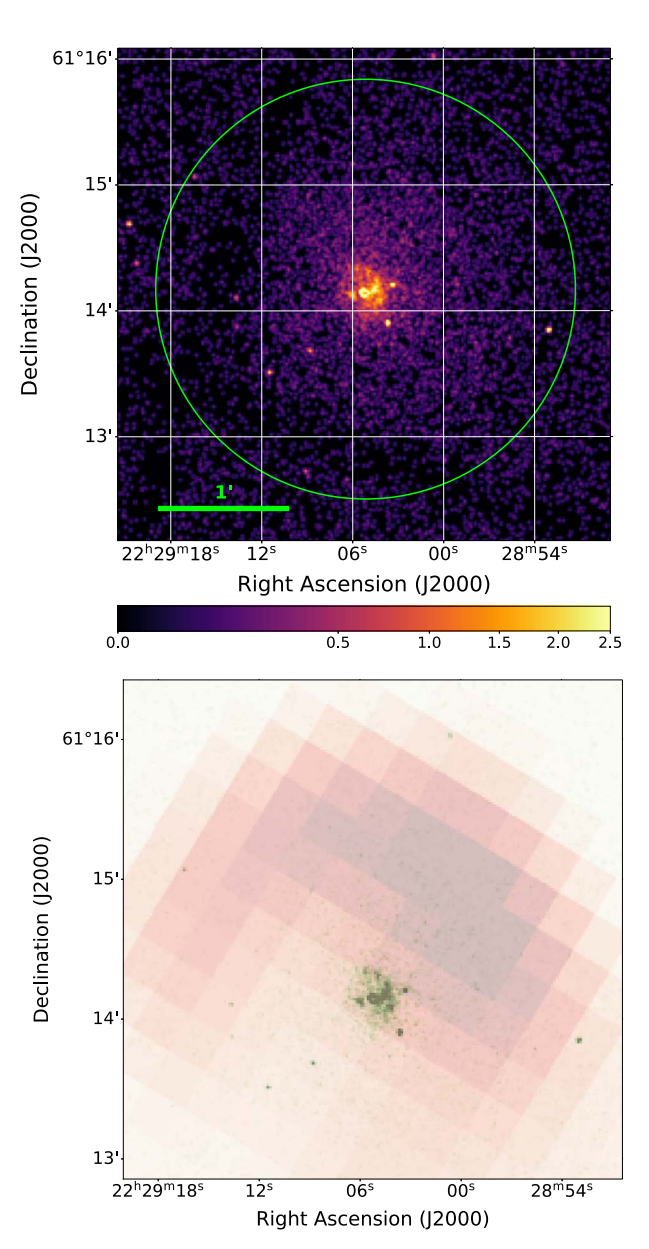


Figure 3. Top: Chandra 0.5–8 keV image of the Boomerang PWN, smoothed to $\sigma = \sim 0.\%5$ (1 pixel). The color scale is in units of counts per pixel. An r=1'' circular region around the pulsar was excised in order to accentuate the PWN features. The solid green circular region is an r=100'' circular region around the pulsar position, used for spectral extraction. Bottom: the 0.5–8 keV Chandra image (same as the top panel) is shown here in green, overlain with the CGPS map of 1420 MHz radio temperature brightness of the Boomerang region in red.

which could guide more complex models specialized to the unique characteristics of the Boomerang system. For the radio band, we adopted the flux data from Kothes et al. (2006). We used the Chandra and NuSTAR X-ray spectra after correcting for ISM absorption. Since we applied one-zone SED models, both radio and X-ray spectra were extracted from the same $r\!=\!100''$ region around the pulsar position. The Fermi-LAT flux upper limits were derived from the analyses described in Section 2.2. As the difference between the VERITAS 0.38–30 TeV and 0.72–30 TeV upper limits found in Section 2.3 is small, we chose to use the former value. Note that the source extraction regions for Fermi-LAT and VERITAS analyses are

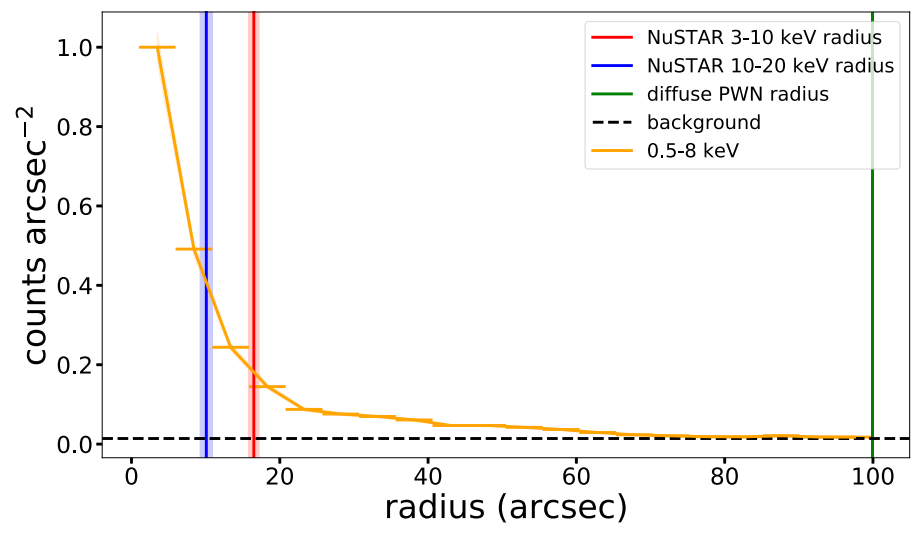


Figure 4. Chandra 0.5-8 keV radial profile of the Boomerang PWN. The vertical lines indicate the PWN radius as measured from the diffuse X-ray emission (green), NuSTAR 3-10 (red), and 10-20 keV (blue) energy bands. The 1σ errors are indicated by the shaded regions. The error bars designate the $\sim 5''$ radial bin widths.

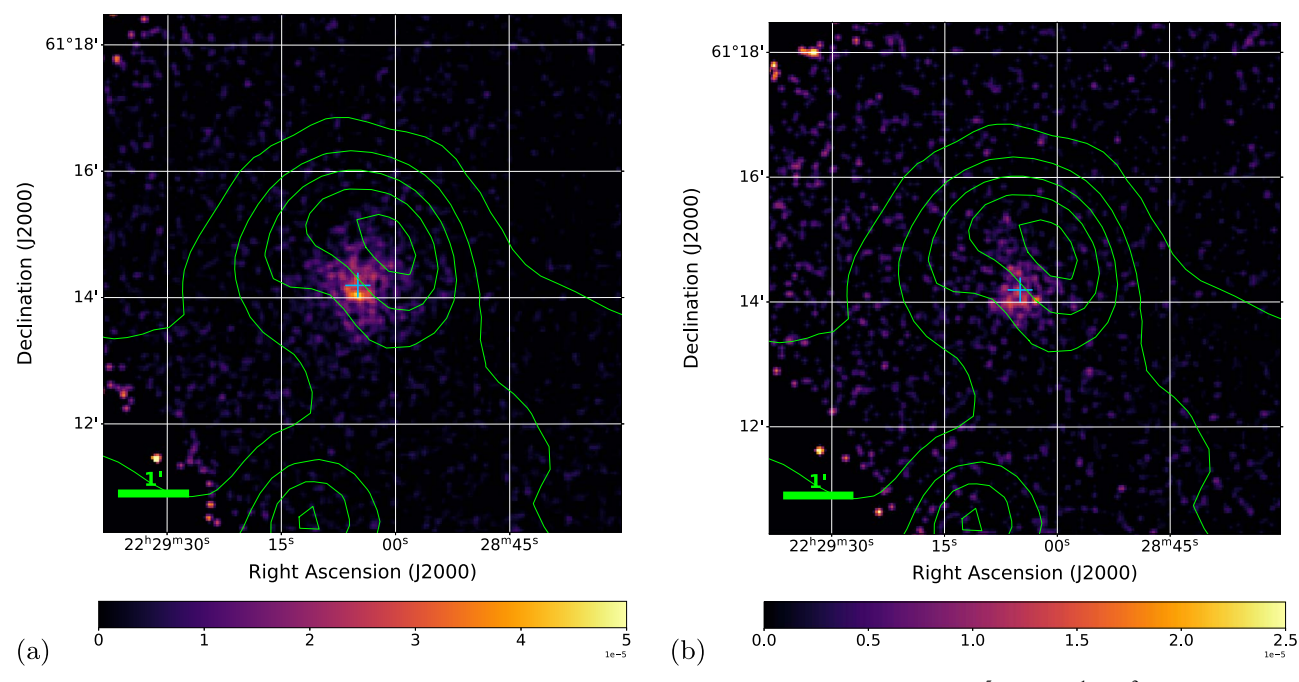


Figure 5. NuSTAR 3–10 keV (a) and 10–20 keV (b) background-subtracted flux images of the Boomerang PWN [10⁻⁵ counts s⁻¹ cm⁻²]. 1420 MHz radio contours are shown in green and the position of PSR J2229+6114 is marked by the blue cross.

subject to the telescope PSF sizes, which are larger than r = 100''. Throughout the SED modeling, we consider two contrasting source distances of 0.8 and 7.5 kpc suggested by the H I velocity (Kothes et al. 2001) and the pulsar's DM measurement (Abdo et al. 2009a), respectively.

Below we present three different SED models. NAIMA models radiative SEDs for a given time-independent electron energy distribution (Section 3.1). Although this is a simplistic approach, we attempt to constrain several PWN parameters such as *B*-field and electron spectral index. In Section 3.2, we applied the time-dependent SED model package GAMERA (Hahn 2016) to the multiwavelength SED data. This time-dependent approach, which assumes free expansion of the

PWN, revealed several challenges in fitting the PWN SED data and size simultaneously, and further constrained multiple PWN properties. However, both NAIMA and GAMERA proved to be overly simplistic. As can be seen from visual inspection of the radio and X-ray flux data, a power-law fit to the X-ray data will undershoot the observed radio data, a phenomenon seen for only a few other PWNe (see Hattori et al. 2020 for example). The best-fit results from both NAIMA and GAMERA confirm the difficulty in reproducing both the radio and X-ray data with such simplistic models. We therefore also considered the PWN evolution using the more complex, dynamical SED model developed by Gelfand et al. (2009) in Section 3.3. The model has been widely used for modeling SED data of various PWNe

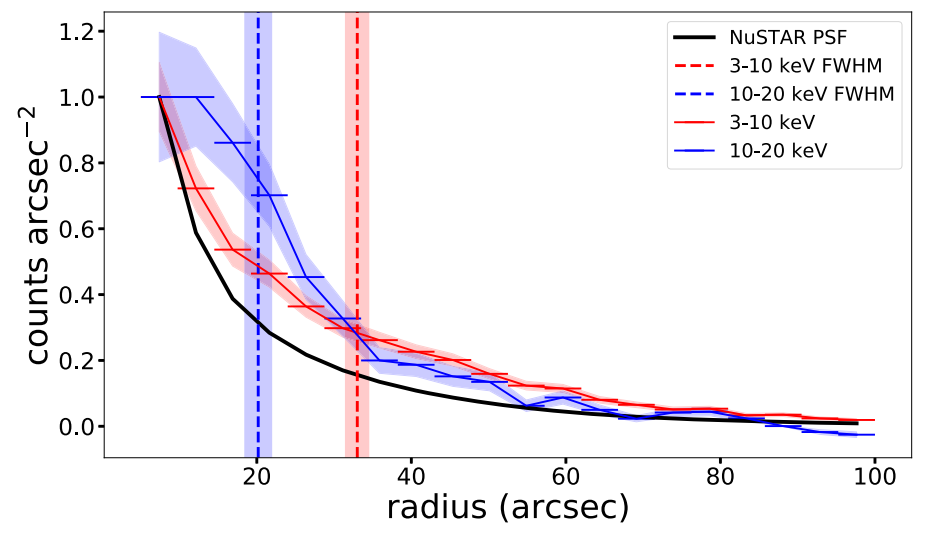


Figure 6. NuSTAR X-ray radial profiles of the Boomerang PWN in the soft (red) and hard (blue) bands, compared to the NuSTAR PSF. The vertical lines indicate the SHERPA best-fit 2D Gaussian FWHM in each energy band. The 1σ errors are indicated by the shaded regions. The horizontal bars designate the $4\rlap...^{\prime\prime}75$ radial bin widths.

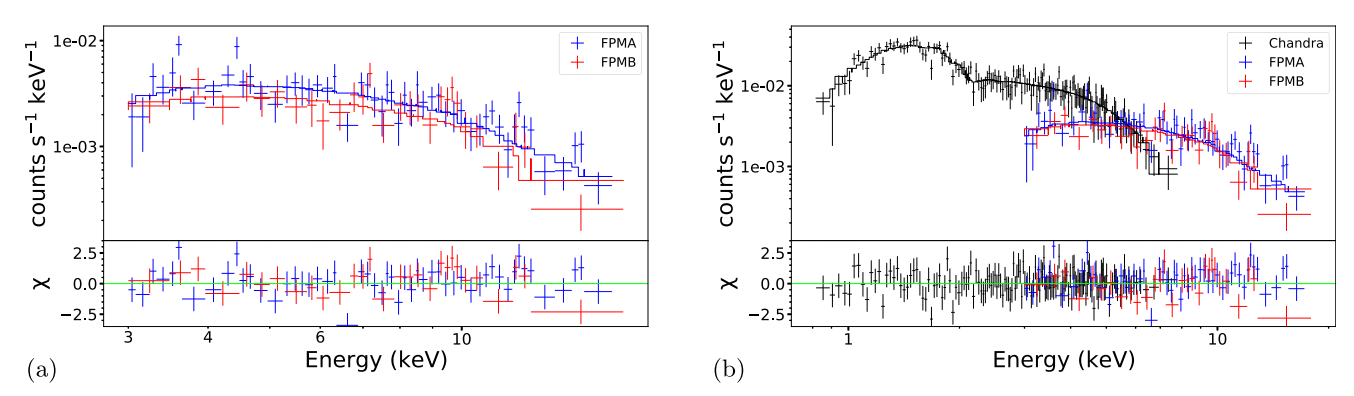


Figure 7. NuSTAR-only spectra (a) and NuSTAR-Chandra joint spectra (b) fit to an absorbed power-law model.

including the Crab nebula, G21.5–0.9, and composite SNR–PWN systems (e.g., Hattori et al. 2020). The dynamical PWN model allowed us to track a full evolution path from the free expansion, SNR reverse shock interaction, and re-expansion phases. Both the SED and PWN radius are modeled as functions of time in comparison with the observation data. In this physically motivated approach, we determine the current *B*-field, the pulsar's true age, its expansion velocity, and its current evolutionary stage.

3.1. NAIMA SED Model

In order to estimate initial PWN parameters from the SED data, we relied on the NAIMA V0.10.0 Python package (Zabalza 2015). NAIMA is a time-independent, one-zone SED model used to generate multiple radiative model components from an assumed particle energy distribution. We fit the multiwavelength SED data assuming that the electron distribution is in the form of a power-law model $A(E_{\rm e}/E_0)^{-p}$ between $E_{\rm e}=E_{\rm min}$ and $E_{\rm max}$. While a hard cutoff at $E_{\rm e}=E_{\rm min}$ is not physically motivated, it is implemented to simplify the model. We generated leptonic radiation models with synchrotron radiation, ICS, and synchrotron self-Compton (SSC) components. We adopted the cosmic microwave background (CMB)

as a seed photon source for the ICS component. No IR seed photons were added so as to maintain the ICS component of the model as a lower limit. Furthermore, including a variable IR seed photon component would only add to the model's degeneracies, an already significant issue which we discuss below. We consider an IR photon field in the more elaborate dynamical model in Section 3.3. While the initial estimates of the physical parameters of the emitted plasma provided by NAIMA are useful, the model does not directly provide any insight into where this emitting plasma came from, and—due to the evolution of the PWN inside the SNR, especially once it collides with the reverse shock—the particle spectrum is unlikely to be well described by a single or broken power law. Our fitting results confirm NAIMA's inadequacy in describing the Boomerang PWN's particle spectrum.

We first focused on reproducing the radio spectral break at \sim 5 GHz and X-ray spectra. We found that the radio data are adequately fit by various sets of B and E_{\min} values, as listed in Table 4. We have shown that the radio spectral break can be caused by the selected E_{\min} . The origin of the break in the electron spectrum, used here to fit the radio break, cannot be determined with the model. Given the degeneracy between B and E_{\min} , we did not find B=2.6 mG as a unique solution to reproduce the radio data, contrary to the results of Kothes et al.

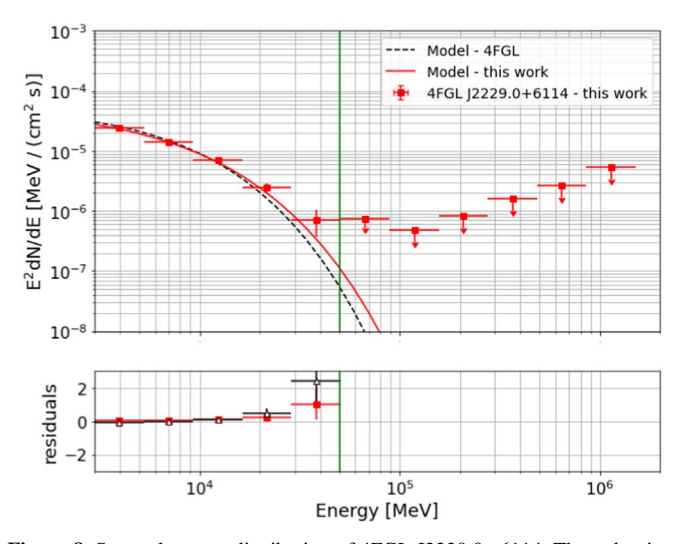


Figure 8. Spectral energy distribution of 4FGL J2229.0+6114. The red points and upper limits were derived from the analysis of LAT data presented in this work. The red solid line indicates the best-fit model to the data points, while the black dashed line is the same spectral model, with the best-fit parameters reported in the 4FGL catalog. The inset reports the residuals as (data – model)/model, for the best-fit model derived from this work and the 4FGL catalog one. The green line denotes the threshold at which we separate the pulsar emission (left) from the nebula emission (right).

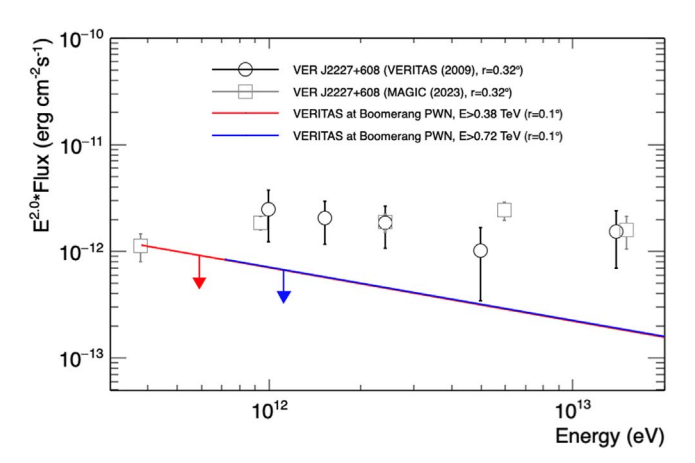


Figure 9. Upper limits of VERITAS at the location of Boomerang PWN with two event selections. VHE gamma-ray emission near the tail region of SNR 106.3+2.7 measured by the IACTs, VERITAS (Acciari et al. 2009), and MAGIC (MAGIC Collaboration et al. 2023) is shown for comparison.

(2006). On the other hand, the electron spectral index was constrained to p = 2.5 by fitting the radio and X-ray spectra with a synchrotron model component. We expect that $(p-1)/2 = \Gamma_x - 1$. We therefore infer from p = 2.5 that $\Gamma_{\rm r} = 1.75$, significantly larger than any of the X-ray photon indices found in Table 2, confirming that NAIMA cannot adequately fit both the radio and X-ray data. However, the parameters serve as an initial estimate. For each assumed source distance (0.8 and 7.5 kpc), a list of the model parameters for four representative cases (including B = 2.6 mG) is shown in Table 4 and two representative SEDs are plotted in Figure 10. In the gamma-ray band, the ICS and SSC components remain below the Fermi-LAT and VERITAS flux upper limits as long as $B > 5 \mu G$. This is because, as the magnetic field is decreased, a larger number of electrons are required to fit the radio and X-ray data and thus enhance the model GeV-TeV flux through the ICS component. If we consider other seed photon sources than the CMB, the lower limit will be higher than 5 μ G.

NAIMA outputs the total energy of the electron population, U_E , integrated between E_{\min} and E_{\max} . Assuming the *B*-field is uniform throughout the interior of the PWN (r < 100''), we calculated the total magnetic field energy as $U_B = \frac{B^2}{8\pi} \times V_{PWN}$, where $V_{\rm PWN} = (4/3)\pi R_{\rm PWN}^3$ is the volume of the PWN. The total electron and magnetic field energies for each fit are provided in Table 4. Given the constraints on the synchrotron radiation fluxes, increasing the magnetic field from $B \sim 1 - 10 \,\mu{\rm G}$ to $B \gtrsim 100 \,\mu{\rm G}$ requires decreasing the electron density dramatically. As a result, the fraction of the total energy allocated to the PWN B-field (η_B) is ~ 1 for $B \gtrsim 100 \,\mu\text{G}$. Such a high magnetization parameter is unusual if compared to other PWN systems—e.g., Martin et al. (2014) found $\eta_B = 7 \times$ 10⁻⁴–0.02 from six PWNe including the Crab nebula (which possesses the highest η_B value). If we attain an η_B value comparable to those deduced from the other PWNe, it points to a lower B-field range of $B \lesssim 10 \,\mu\text{G}$. While these arguments as well as the suggested B-field range $(B \sim 5-10 \,\mu\text{G})$ are empirical based on the time-independent one-zone SED model fitting, we will address this issue with more advanced SED models and other X-ray analysis results in the later sections.

3.2. GAMERA SED Model

To further characterize the PWN properties, we modeled the time evolution of the particle distribution and radiation SED using GAMERA (Hahn 2016). GAMERA allows us to inject leptons and track their energy distribution as they vary via radiative and adiabatic cooling over time. However, the GAMERA modeling does not account for the interaction between the PWN and the parent SNR, which makes the PWN compress and expand, altering the injected particle distribution significantly. The model assumes that the PWN is expanding with a constant velocity, and thus only tracks the recent PWN evolution. The age reflects the time since the PWN started expanding, whether that be from the time of the pulsar's birth or from the time that the reverse shock passed through the PWN. We assumed R_{PWN} increased linearly with time over the short lifetime of the new PWN and matched its current radius (at $t = t_{PWNage}$) with the measured radio PWN size. Assuming two different source distances (0.8 and 7.5 kpc), we adopted the corresponding PWN sizes of r = 0.4 and 4 pc. We assumed continuous particle and magnetic field injection into the PWN at the rate of the pulsar's current spin-down power $\dot{E} = 2.2 \times 10^{37} \text{ erg s}^{-1}$. A fraction of the spin-down power (η_B) is injected into the PWN in the form of magnetic potential energy U_B . The magnetic field B was assumed to be uniform throughout the spherical volume of the PWN. The rest of the spin-down power is injected into particle energy following a power-law distribution $A(E/E_0)^{-p}$. The normalization factor A is determined by the total particle energy of $(1 - \eta_g - \eta_B)\dot{E}$ where η_{e} is the gamma-ray efficiency of the pulsar. We ignored the fraction of the spin-down energy allocated to gamma-ray pulsations; this contribution should not significantly affect the model outputs. The injected particle distribution is evolved by three particle cooling mechanisms, i.e., adiabatic, synchrotron, and ICS components. The adiabatic cooling rate is calculated using the expansion velocity of the PWN, which we assumed to be constant ($v_{PWN} = R_{PWN}/t_{age}$). We then calculated a radiation SED from the particle distribution at $t = t_{age}$. We employed a

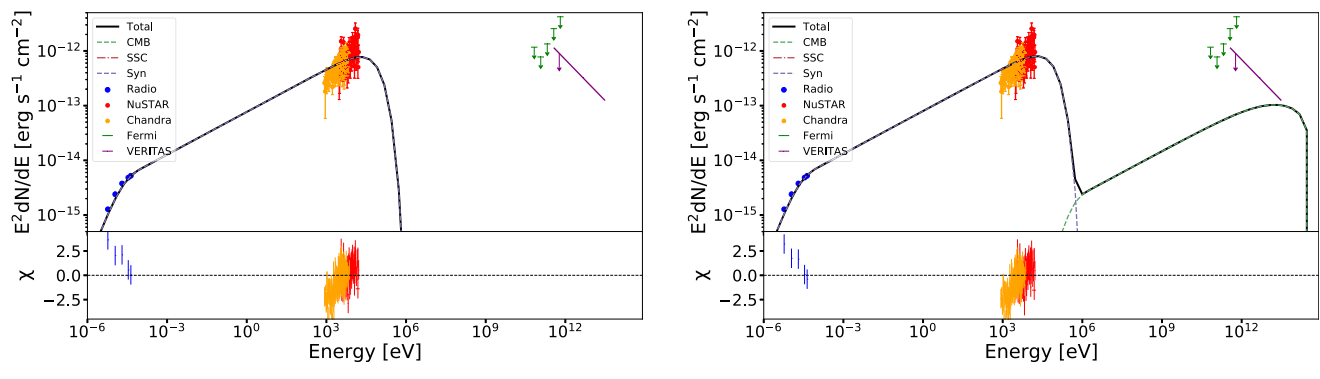


Figure 10. NAIMA simple power-law SED fits with the B-field set to 2.6 mG (left) and 5 μ G (right). The complete set of parameters for each fit, as well as for other B-field scenarios, is shown in Table 4.

 Table 4

 Fit Parameters from Various Leptonic NAIMA Model Cases

Distance (kpc)	$B(\mu G)$	p	E_{\min} (GeV)	$E_{\rm max}$ (TeV)	Electron Energy (erg)	Magnetic Field Energy (erg) ^a	η_E	η_B
0.8	2600	2.5	0.32	22	2.3×10^{41}	2.0×10^{48}	~0	~1
0.8	100	2.5	1.64	120	2.9×10^{43}	2.9×10^{45}	0.01	0.99
0.8	10	2.5	5.18	400	1.0×10^{45}	2.9×10^{43}	0.97	0.03
0.8	5	2.5	7.33	500	2.8×10^{45}	7.3×10^{42}	0.998	0.002
7.5	2600	2.5	0.32	22	2.0×10^{43}	1.6×10^{51}	~0	~1
7.5	100	2.5	1.64	120	2.5×10^{45}	2.9×10^{48}	0.001	0.999
7.5	10	2.5	5.18	400	9.1×10^{46}	2.9×10^{46}	0.76	0.24
7.5	5	2.5	7.33	500	2.5×10^{47}	7.3×10^{45}	0.97	0.03

Note.

leptonic radiative model comprising emission from synchrotron radiation and ICS of the CMB and synchrotron self-Compton scattering emission. Similarly to our NAIMA fitting, we have only taken ICS of CMB and SSC components into account to maintain the ICS component of the model as a lower limit. Still, GAMERA is not able to describe the data very well as summarized below. Adding other potential seed photons, such as IR, would only make fitting the data more challenging for these models, as the IC component would encroach on the Fermi-LAT and VERITAS upper limits. The addition of an IR component is considered for our dynamical model in Section 3.3.

We also attempted to constrain our model based on the lack of X-ray variability over the last $\sim\!20\,\mathrm{yr}$ (Section 2.1.3). Since the luminosity of synchrotron radiation is proportional to B^2 , a sizable variation in B-field can lead to detectable X-ray flux variability. As the PWN evolves, decreasing B-field and increasing particle density cancel each other out and result in a slower evolution of synchrotron luminosity, while ICS luminosity keeps increasing as more particles are injected over time. While fitting the GAMERA model to the multiwavelength SED data, we tracked the evolution of the synchrotron X-ray luminosity $L_{\rm syn}(t)$ and found solutions without significant X-ray variability over the last $\sim\!20\,\mathrm{yr}$.

The best-fit parameters are listed for the cases of short and long distance in Table 5. Figures 11 and 12 show time series of the particle SED, radiation SED, and magnetic field, along with the radiation SED at the current time using the best-fit parameters. Note that both GAMERA models grossly misrepresent the spectrum in the X-ray region and have other shortcomings as discussed below.

(1) d = 0.8 kpc. The lifetime of the PWN should be $t_{\rm age}\sim 30~{\rm yr}$ for $d=0.8~{\rm kpc}$. If $t_{\rm age}\lesssim 20~{\rm yr}$, the model predicts that the 2002 Chandra observation should have detected a much higher X-ray flux than it did. If the lifetime is longer than $\tau \sim 30$ yr, too many leptons are injected into the PWN to be consistent with the GeV and TeV flux upper limits. Currently, the B-field should be as low as $B \sim 2\mu G$ (with a very low magnetization of $\eta_B = 7 \times 10^{-5}$). Otherwise, the model overpredicts synchrotron radiation fluxes in the radio and X-ray bands. We also found that E_{\min} is well constrained by the radio spectral break and the overall flux normalization of electrons (which depends sensitively on E_{\min} for a given \dot{E} and lifetime). The expansion velocity should be high $(V_{PWN} = 1.9 \times$ 10⁴ km s⁻¹) in order to reach the observed PWN radius within \sim 30 yr. To relax these stringent constraints, we introduced an extra, nonradiative energy loss term in GAMERA via escaping leptons. Only if we assumed a short particle escape time $(t_{\rm esc} < 0.05 \text{ yr})$ were we able to fit the SED data with higher η_B values and older ages. However, such a short particle escape time is unrealistic as it is shorter than the light-crossing time of the PWN.

(2) d=7.5 kpc. In contrast, the larger distance allows the PWN to radiate away its rotational energy over a more extensive period of time. For example, over 1000 yr significantly more particle energy can be injected, totaling 3.1×10^{47} erg. While the spectral parameters of injected electrons such as p, $E_{\rm min}$, and $E_{\rm max}$ are similar in the two distance cases (Table 5), η_B is higher at 1×10^{-2} while the current B-field is $4.5~\mu{\rm G}$. The expansion velocity is $3.9 \times 10^3~{\rm km\,s^{-1}}$, which is more in line with the observed PWN velocities

 $^{^{}a}$ η_{E} and η_{B} are calculated by dividing the electron and magnetic field energies by their sum, respectively.

 $(v_{\rm PWN} \sim 1000-1500~{\rm km~s}^{-1})$ from the Crab nebula and Kes-75 (Bietenholz et al. 1991; Reynolds et al. 2018).

Overall, we found that the larger distance allows for an older age (i.e., longer particle injection time) and higher magnetization parameter. In either case, the current B-field needs to be as low as $B \sim 5 \mu G$ in order to match the low radiation efficiency $(L_{\rm syn}/\dot{E})$. Consequently, the radio spectral break cannot be caused by synchrotron cooling at B=2.6 mG as suggested by Kothes et al. (2006). Alternatively, we found that the radio break energy is directly related to the minimum energy $(E_{\rm min})$ in the injected particle energy distribution. Unlike the NAIMA model, the added complexities of the GAMERA model broke the degeneracy between B and $E_{\rm min}$. In both cases, $E_{\rm min} \sim 10$ GeV fit the radio SED data well, and thus we attribute the break to the PWN's intrinsic particle injection distribution.

3.3. Dynamical Model of PWN Evolution

In this section, we explore the time evolution of the Boomerang PWN using the dynamical PWN model (Gelfand et al. 2009). The SED model takes input parameters for the PWN, the SNR, and its environment. This model evolves a homogeneous spherical bubble of relativistic electrons and magnetic field, injected according to the pulsar spin-down luminosity and its evolution, following the dynamics of its expansion into first the expanding ejecta of a spherical SNR, and including the eventual compression by the returning reverse shock and subsequent expansion into the interior of a Sedov blast wave. More details on the model description and applications to other PWNe can be found in Gelfand et al. (2009), Gelfand (2017), Hattori et al. (2020), and Burgess et al. (2022). The physically motivated model tracks the time evolution of the particle energy distribution, radiative SED, and PWN properties (e.g., B and R_{PWN}) by considering particle injection and energy loss due to radiative and adiabatic cooling at each time step. The size and bulk velocity of the PWN are calculated from the pressure balance between the pulsar wind and SNR ejecta. Setting up each model run begins with determining the pulsar's properties. Given the observed current spin-down power \dot{E} (= 2.2×10^{37} erg s⁻¹) and characteristic age $t_{\rm ch}$ (=11 kyr), we first derive the system's true age ($t_{\rm age}$) and initial spin-down luminosity \dot{E}_0 :

$$t_{\rm age} = \frac{2t_{\rm ch}}{p-1} - \tau_{\rm sd} \tag{1}$$

$$\dot{E}_0 = \dot{E} \left(1 + \frac{t_{\text{age}}}{\tau_{\text{sd}}} \right)^{\frac{p+1}{p-1}},\tag{2}$$

where p and $\tau_{\rm sd}$ are the pulsar's braking index and spin-down timescale, respectively. These input parameters fully characterize the pulsar as a particle injection source.

In the model, the pulsar injects leptons and magnetic field at each time step by partitioning the time-dependent spin-down power $\dot{E}(t)$ into $(1-\eta_B)\dot{E}(t)$ and $\eta_B\dot{E}(t)$, respectively. The allocated electron energy is distributed between $E_{\rm e}=E_{\rm min}$ and $E_{\rm max}$ following a broken power-law model. The evolution of both SNR forward and reverse shocks is separately calculated by going through the free expansion and Sedov–Taylor phases. The density profile of SNR ejecta, which follows $\rho_{\rm ej}(r) \propto r^{-9}$ until reaching the density of the ISM, is used to calculate the pressure balance between the pulsar wind and ejecta. The ISM density affects the timescale of the SNR evolution and SNR

Table 5
Model Parameters for the Case Presented in Section 3.2

Parameter	d = 0.8 kpc	d = 7.5 kpc
Age [yr]	30	1000
p	2.4	2.4
E_{\min} [GeV]	7.9	10.0
$E_{\rm max}$ [PeV]	1.0	1.0
$\eta_g^{\; \mathrm{a}}$	1×10^{-3}	7×10^{-2}
η_B	7×10^{-5}	1×10^{-2}
B [μG]	2.1	4.5
Electron energy [erg]	8.9×10^{45}	2.9×10^{47}
Magnetic field energy [erg]	1.3×10^{42}	6.3×10^{45}
Expansion velocity [km s ⁻¹]	1.3×10^{4}	3.9×10^{3}

Note.

reverse shock. After the SNR reverse shock hits the PWN, the ISM density plays an important role as it imposes additional pressure on the pulsar wind. These pressure factors determine the size and bulk velocity of the PWN at each time step. The injected leptons lose their energy via radiative and adiabatic cooling as the PWN expands over time. The radiative cooling in the model takes into account synchrotron and ICS components, which are provided as radiative SED model output. At some point, the SNR reverse shock reaches the PWN and compresses it to the point where the pulsar wind and reverse shock are in a pressure equilibrium before the PWN begins expanding again.

We aimed to reproduce both the multiwavelength SED data and PWN size with the dynamical model. We note that the flux upper limit obtained by VERITAS changes depending on the assumed spectral index (see Table 3). For the dynamical SED fitting, we used the VERITAS upper limit at the decorrelation energy because the sensitivity of the limit to changes in the spectral index is lowest at this energy. As shown in Figure 13, we considered the upper limit optimized for 2% of the Crab Nebula strength for the model fitting, where the decorrelation energy is 1.12 TeV. As we did for the NAIMA and GAMERA model fitting, we considered the case for both d = 0.8 and 7.5 kpc below. We initially only use the CMB as a seed photon source for the ICS component; we then test the effect of adding an IR field to the model. We recognize that the detailed radio and X-ray structure of the PWN (pulsar with small X-ray nebula in the interior of the boomerang-shaped radio arc) is not well represented by a homogeneous sphere, but as with the two previous models, we hope to obtain some general insight into the possible nature and evolution of the PWN with this tool.

(1) d=0.8 kpc. Given the very low radiation efficiency $(L_{\rm radio}/\dot{E}=3\times10^{-8} {\rm and}\ L_{\rm X}/\dot{E}=7\times10^{-6})$, it is extremely difficult to allocate the pulsar's expended rotational energy without overshooting the flux data. To suppress the synchrotron radiation in the radio and X-ray bands, we need to minimize the number of injected leptons and the PWN *B*-field. We were able to satisfy both the low radiation efficiency and compact PWN size $(r=0.4\,{\rm pc}\ {\rm at}\ d=0.8\,{\rm kpc})$ with the following (Case A) SED model. For $d=0.8\,{\rm kpc}$, any free-expansion phase solution that matched the flux data largely overestimated the PWN size. We therefore had to consider a reexpanding PWN after its interaction with the SNR reverse shock. We were able to roughly reproduce all the radio, X-ray, and gamma-ray fluxes by allocating the particle energy to the

^a The gamma-ray efficiency of PSR J2229+6114 from Abdo et al. (2009a). f_{Ω} (Equation (3) in the cited work) was assumed to be 1.

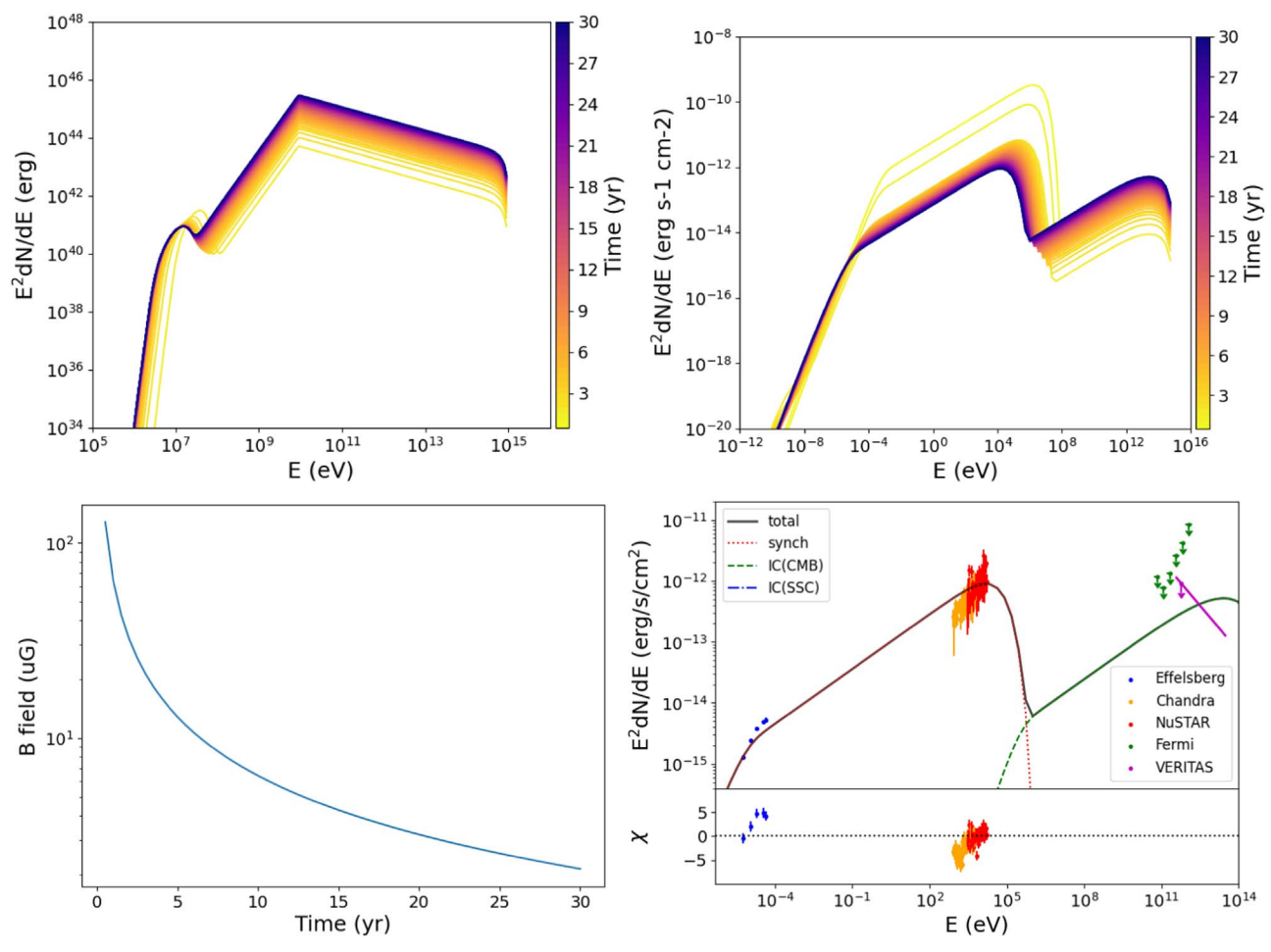


Figure 11. Time evolution of the lepton (top left) and radiation (top right) SEDs, and *B*-field (bottom left) and the radiation SED at the current time (bottom right) assuming d = 0.8 kpc.

unobserved energy bands such as MeV and >100 TeV energies. We arrived at a very low η_B and high ISM density. The predicted PWN radius (r = 0.35 pc) is roughly consistent with the size of the Boomerang PWN. However, the predicted X-ray spectral shape is not consistent with the NuSTAR data and also requires an extremely high braking index (p = 5.6) or very young pulsar age ($t_{age} = 640 \text{ yr}$). While the Case A model almost works for reproducing the observation data, we do not consider it compelling due to the unreasonable parameter values. For example, the SNR's interaction with the high ISM density in Case A (160 cm⁻³) at a distance of 0.8 kpc and age of 640 yr would produce the brightest thermal SNR ever observed by a large factor. Under the assumption that the PWN confines all of the leptons injected over its entire lifetime, it is nearly impossible to model the observed PWN's faint emission if the source distance is 0.8 kpc.

(2) d=7.5 kpc. Despite the larger distance, we still find it constraining to fit the SED data and PWN size simultaneously. Below we present two different cases: (1) a young PWN in the free-expansion phase (Case B) and (2) a re-expanding PWN after SNR crush (Case C). Both cases have the same number of free parameters. In both cases, we need to evolve the PWN size to match $r \sim 4$ pc while keeping the number of injected leptons to the level required for fitting the radio, X-ray, and gamma-ray SED data. The third column in Table 6 and Figure 13 (upper right panel) show the model parameters and SED plot, respectively, for Case B. This case assumes that the PWN

has been expanding over 1.8 kyr, and it is similar to the GAMERA model for d = 7.5 kpc. As Figure 14 (upper panels) shows, the current B-field is 3.7 μ G while the PWN expanded to r = 3.8 pc. Note that the power-law spectral index is softer below than above E_{break} in Case B, which is highly unusual, but has been seen in a few other cases (Temim et al. 2015; Hattori et al. 2020). The spectral break at the highest radio flux point in Model B is caused by the minimum energy of the particles injected at the termination shock. Below this energy, all of the particles were injected earlier and cooled to this regime. Above this energy, there are a mix of particles injected earlier which have cooled, and freshly injected particles that have not had time to cool yet. The energy spectra of these two populations of particles are different, which leads to a change in slope at the energy separating the two. As can be seen in Figure 13, Case B fits the X-ray data well, while a clear trend away from the model can be seen in the plot of residuals in the radio band. Since the emission in the radio band is dominated by lowenergy particles, this discrepancy between data and model may be due to our simplified assumption that E_{\min} stays constant over time. In contrast to Case B, Case C represents the SNR crush scenario, as was suggested by Kothes et al. (2006). We evolved the PWN through the reverse shock crush into reexpansion over $t_{age} = 2.1$ kyr, as indicated by the plot of PWN radius over time in Figure 14 (lower panels). The current Bfield and PWN radius are 2.5 μ G and 2.9 pc, respectively. As seen in Figure 13, the model fits the data well. While slightly

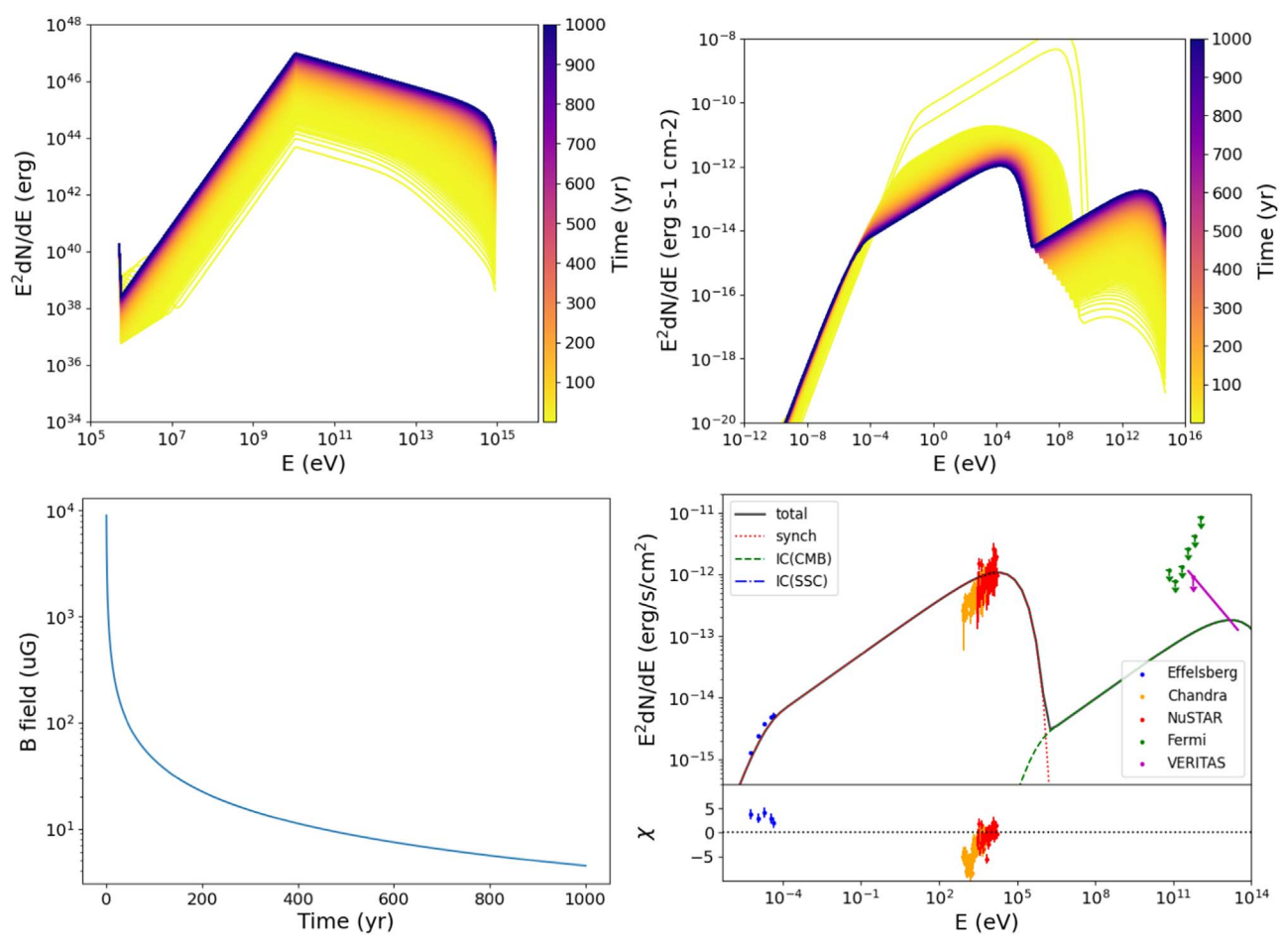


Figure 12. Same plot as Figure 11 but for d = 7.5 kpc.

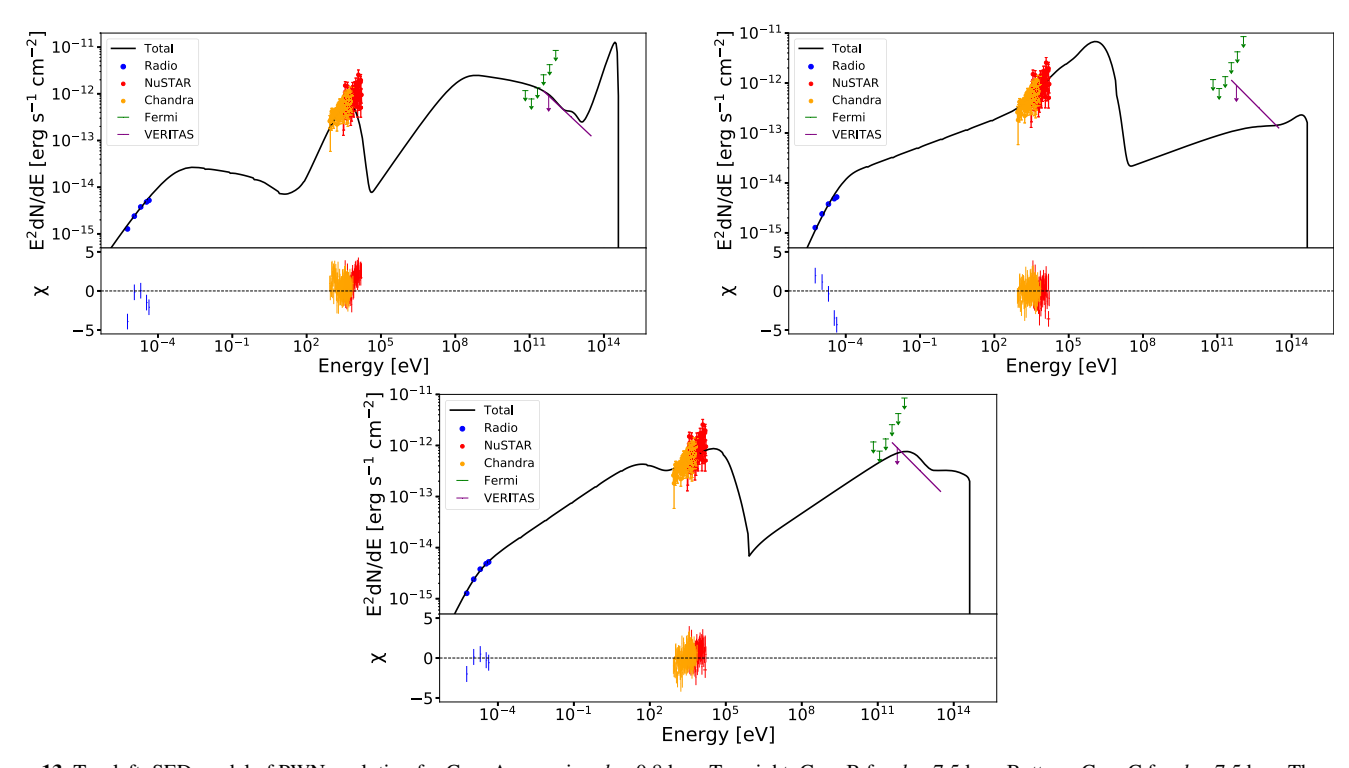


Figure 13. Top left: SED model of PWN evolution for Case A assuming d = 0.8 kpc. Top right: Case B for d = 7.5 kpc. Bottom: Case C for d = 7.5 kpc. The model parameters for these cases can be found in Table 4.

overshooting the VERITAS upper limit, factoring in the \sim 20% uncertainty in the upper limit of the TeV photon density at the decorrelation energy due to the unknown photon index in this band, the model is consistent with the nondetection by VERITAS. Given how close the minimum and break particle energies are, the model favors a single power-law injection spectrum with $p \sim 2.3$ (i.e., standard Fermi).

Reproducing the gamma-ray emission of many PWNe often requires background photon fields in addition to the CMB from either surrounding dust (e.g., G21.5-0.9; Hattori et al. 2020) and/or nearby stars (e.g., HESS J1640-465 and Kes-75; Abdelmaguid et al. 2022; Straal et al. 2023). Since the gammaray emission from the Boomerang has not been detected, the presence of additional background photon fields cannot be directly constrained by the modeling above. Therefore, to determine their possible effect on the parameters derived above, we modeled the SED and dynamical properties of this source assuming an additional photon field with a temperature T = 30 K and energy density $5 \times$ that of the CMB, typical values for warm dust in these systems (Cox et al. 1986; Torres et al. 2013). As shown in Table 6, for Case B' we can reproduce the properties of the Boomerang for a set of model parameters similar to those of Case B (where the only background photon field is the CMB). However, in our parameter exploration we were not able to reproduce the observed properties of the Boomerang, assuming this additional background photon field, for a set of parameters similar to Case C in Table 6. This does not necessarily exclude Case C as a reasonable description for the Boomerang, since there are many regions in the Galaxy where the energy density of dust emission is less than that of the CMB (e.g., G21.5-0.9; Strong et al. 2000).

Overall, the PWN evolution model does not reproduce both the SED data and PWN size with reasonable parameters if we assume d = 0.8 kpc. In all of the SED models presented in this section, we found $B \sim 2-4 \mu G$. Alternatively, we found that an extremely magnetized PWN with $\eta_B \sim 1$ can fit the SED data well. More specifically, when we adopt $\eta_B = 0.99$, only 1% of the pulsar's rotational energy is allocated to particle injection and the current B-field is $\sim 100 \ \mu G$. The smaller number of injected leptons and higher B-field cancel each other to fit the synchrotron SED in the radio and X-ray bands. However, such a high magnetization parameter is unusual compared to those of six other PWNe ($\eta_B = 7 \times 10^{-4}$ –0.02) including the Crab nebula (Martin et al. 2014). For the case of d = 7.5 kpc, we consider Case C more plausible since Case B and Case B' suggest that the high-energy particle index is greater than the low-energy particle index. Furthermore, in Case C the PWN interacts with the SNR reverse shock, which could explain the offset between the radio and X-ray peak emission. No explanation for this offset can be inferred from Case B or Case B'.

4. Discussion

We discuss constraining the properties of the Boomerang PWN and its recent evolution based on the X-ray and multiwavelength observations. In the previous sections, we examined the hypothesis proposed from the radio observations (Kothes et al. 2006) that the Boomerang is a highly magnetized PWN (B=2.6~mG) crushed by an SNR reverse shock 3900 yr ago, which was made under the assumption that the radio break in Boomerang's spectrum is due to synchrotron cooling.

 Table 6

 Model Parameters for the Four Cases Presented in Section 3.3

Model Parameter	Case A	Case B	Case B'	Case C
Source dis- tance [kpc]	0.8	7.5	7.5	7.5
SN explosion energy [erg]	3.0×10^{50}	3.6×10^{51}	4.0×10^{51}	1.9×10^{51}
SN ejecta mass $[M_{\odot}]$	1.6	4.2	4.9	2.0
ISM density [cm ⁻³]	160	0.3	0.3	0.9
Magnetic field	1.5	3.7	2.9	2.5
strength [μG]				
PWN radius [pc]	0.35	3.8	4.6	2.9
Pulsar braking index	5.6	2.9	2.8	3.1
Pulsar spin-down timescale [kyr]	3.9	8.9	9.1	7.7
True age [kyr]	0.64	1.8	2.2	2.1
Initial spin-down power [erg s ⁻¹]	2.7×10^{37}	2.2×10^{37}	3.4×10^{37}	3.5×10^{37}
Wind magnetization (η_B)	8×10^{-8}	0.006	0.005	0.0007
E_{\min} [GeV]	0.4	22.3	20.0	8.7
$E_{\rm max}$ [PeV]	0.2	4.0	3.5	1.2
$E_{\rm break}$ [TeV]	0.14	335.77	300.00	0.01
p_1	1.5	2.6	2.6	1.6
p_2	3.1	1.3	1.3	2.3

Note. The SED plots for Case A, Case B, and Case C are shown in Figure 13. The parameters p_1 and p_2 are the particle indices below and above E_{break} , respectively.

However, the radio break is not necessarily caused by synchrotron cooling, which may explain the discrepancy between the results in this paper and those from Kothes et al. (2006).

Below, we present some implications for this composite SNR-PWN system, especially in the head region, and suggest future observations to further elucidate the origin of the head-tail morphology and UHE emission.

4.1. Constraining PWN Magnetic Field

As shown in Section 3, our SED study strongly suggests that the current *B*-field should be $B \lesssim 3\mu G$, otherwise the observed synchrotron fluxes will be significantly overpredicted. Combined with the results of the GAMERA SED model in Section 3.2, below we consider the energy-dependent X-ray size measurements from the NuSTAR observation and constrain the PWN B-field. The smaller X-ray size (e.g., r = 20'' in 10–20 keV) compared to the radio size (r = 100'') is often observed for other PWNe (Coerver et al. 2019). The size of the radio nebula usually reflects the PWN size determined by the evolution of particle flow over the pulsar's age. In contrast, the smaller X-ray size is determined by the synchrotron cooling time. The synchrotron cooling time for electrons emitting X-rays of energy E [keV] is $\tau_{\rm syn} = 1.2 B_{\rm mG}^{-3/2} E_{\rm keV}^{-1/2}$ yr (Reynolds et al. 2018). Since the synchrotron cooling time depends on electron energy, we expect X-ray PWN size to shrink with photon energy. The synchrotron burn-off effect is evident, as we measured different X-ray sizes in two energy bands—33" (3-10 keV) and 20" (10-20 keV). Assuming a constant flow velocity over the X-ray synchrotron cooling time, the ratio of the PWN radii between the hard and soft energy bands should be approximately equal to the ratio between the

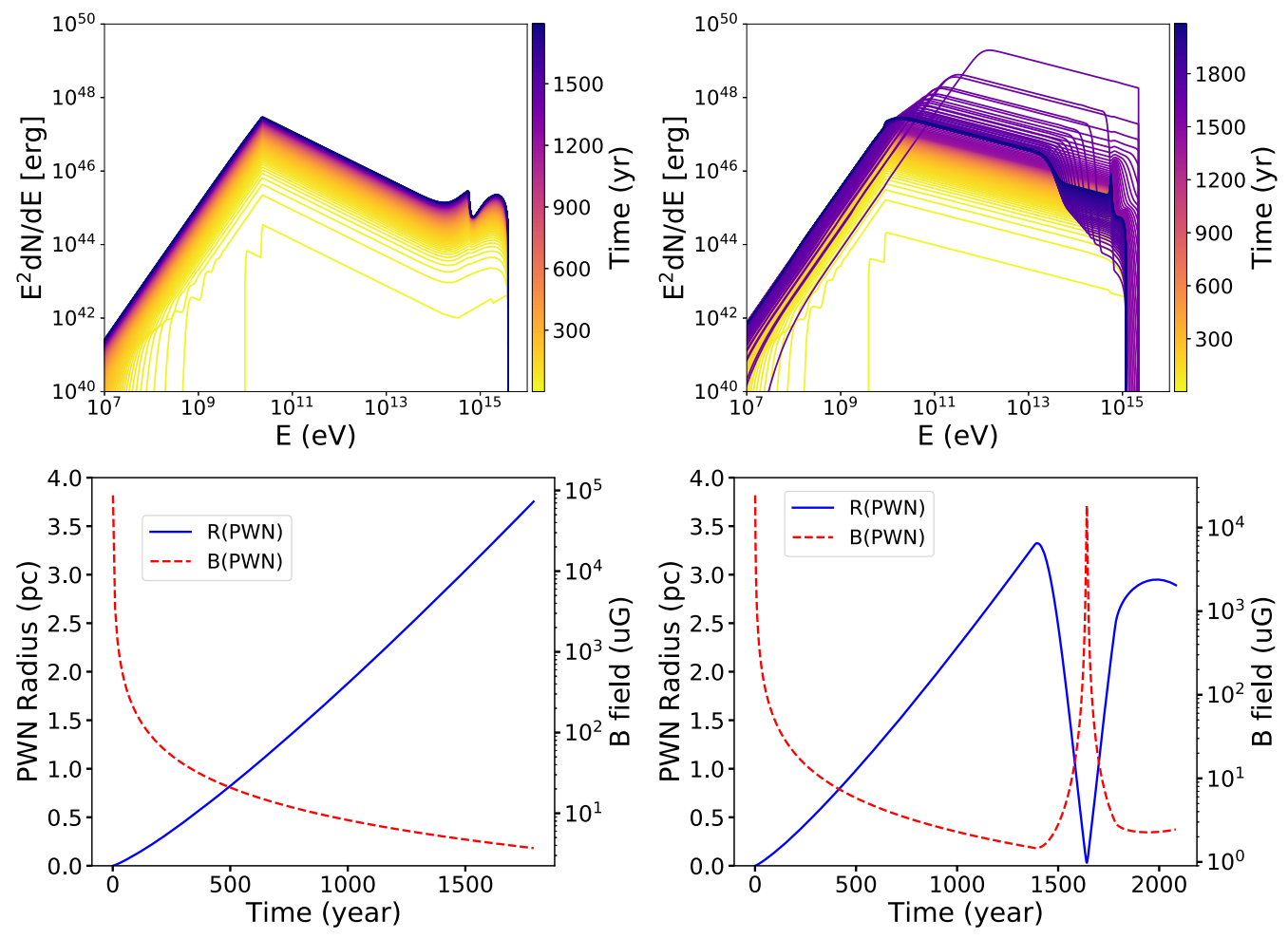


Figure 14. Top: electron evolution for Case B (left) and Case C (right) of Figure 13 and Table 6. Bottom: evolution of R_{PWN} and magnetic field of Case B (left) and Case C (right).

synchrotron cooling times for the respective mid-band energies. Subsequently, adopting the middle energy in each band (6.5 and 15 keV), we estimate that the PWN size ratio between the two energy bands should be 1.5 if the flow velocity is constant, which is close to the observed ratio of 1.7. Hence, we consider the hypothesis of constant flow velocity as viable.

Assuming a source distance of 7.5 kpc (as suggested by the pulsar's DM measurement and supported by our SED model fitting), the X-ray angular sizes in the 3-10 and 10-20 keV bands correspond to PWN radii of $r \sim 0.7$ pc and ~ 0.4 pc, respectively. As expected, these radii are significantly smaller than the PWN radius assumed for the SED modeling (\sim 4 pc at d = 7.5 kpc), which represents the size of the PWN in the radio band. For a given B-field, we can derive an upper limit of the PWN size assuming that leptons moved outward at the speed of light during their lifetime. Using the synchrotron lifetime for the highest-energy X-ray emission ($E_{\gamma} = 20 \text{ keV}$), the hard X-ray PWN size of r = 0.4 pc sets an upper limit of B <0.35 mG, which is lower than the B-field value suggested by Kothes et al. (2006). We can further constrain the B-field with a more realistic estimate of the PWN flow velocity. For example, multiepoch Chandra X-ray observations of Kes-75 measured an expansion of the PWN at $V_{\rm PWN} \sim 1000 \ {\rm km \ s^{-1}}$ or $3.3 \times 10^{-3} c$ (Reynolds et al. 2018). The Crab nebula is known to expand at a velocity of $V_{\rm PWN} \sim 1500~{\rm km\,s^{-1}}$ (Bietenholz et al. 1991) and its radius increases almost linearly with time— $R(t) \propto t^{1.264}$

(Bietenholz & Nugent 2015). If we adopt these flow velocities, the hard X-ray size of the Boomerang PWN in the 10–20 keV band suggests $B \sim 7$ –10 μ G. We also estimated a range of the flow velocity using the output data on the evolution of the PWN size (i.e., R(t)) provided by the dynamical PWN model (Section 3.3). We found $v_{\rm PWN} \sim 2400~{\rm km\,s^{-1}}$ and $\sim 400~{\rm km\,s^{-1}}$ over the last 60 yr of expansion for Cases B and C, respectively, and their evolution of PWN radius is shown in Figure 14. These PWN velocities yield $B \sim 6$ –14 μ G, which is slightly higher than the B-field suggested by the dynamical model fitting in Section 3.3.

Our estimates for the PWN B-field, based on the PWN's X-ray spatial properties and SED fitting, are not only significantly below what was suggested by Kothes et al. (2006) but also below $B=140\,\mu\text{G}$, which was suggested by Liang et al. (2022) based on modeling of the diffusion of relativistic electrons in the PWN. Our disagreement with the B-field derived from the analysis done by Liang et al. (2022) is expected given our different assumptions and models. While Liang et al. (2022) incorporated UHE tail emission not necessarily related to the PWN itself within their SED modeling, this paper focuses solely on emission within the general bounds of the PWN region. Furthermore, unlike the dynamical model used in this paper, the PWN model used in Liang et al. (2022) does not include any interaction with the

SNR, and the temporal evolution consists only of changes resulting from diffusion and radiative losses.

4.2. PWN Evolution

The dynamical SED model fitting in Section 3.3 suggests that the Boomerang PWN is currently re-expanding to $r \sim 3$ pc after being crushed by an SNR reverse shock ~1000 yr ago, much less than the pulsar's ~ 10 kyr characteristic age. As can be seen in the Case C scenario of the bottom panels of Figure 14, we note that the PWN is undergoing a small second compression due to an overshoot in its re-expansion, which resulted in a negative pressure differential between the PWN's interior and surrounding material. The Boomerang PWN is powered by a population of fresh electrons injected over the last \sim 1000 yr. After the PWN compression amplified the Bfield to $B \gtrsim 10$ mG, its *B*-field decreased to $B \sim 3 \mu$ G, as of the present day, as a result of the nebula expansion. It is interesting to note the consequence of this temporally varying B-field for the spatial variations of the PWN's spectrum. Particles are generally older further away from their source pulsar (Temim et al. 2015). Subsequently, if the B-field was higher in the past as suggested by the dynamical model, leptons further away from PSR J2229+6114 would generally have experienced more significant synchrotron losses than those found closer to it. Therefore, this decrease in B-field over time may explain the significant softening in the X-ray spectrum shown to occur with increasing distance from the pulsar by Ge et al. (2021).

Hydrodynamic simulation of SNR-PWN interaction exhibited head- and tail-like features in the particle density maps (Figure 2 in Kolb et al. 2017). According to this simulation study, there are two factors that determine the composite SNR-PWN morphology: (1) density gradient and (2) pulsar proper motion.

As suggested by Kothes et al. (2006), the density gradient around the head region likely caused their highly asymmetric morphology and Boomerang-like PWN shape in the radio band. While the X-ray-bright PWN ($r \sim 0.4$ –0.7 pc) should be powered by a population of young electrons injected over the last ~1000 yr, the relic electrons injected prior to the SNR crush should still be producing synchrotron radiation in the radio and X-ray bands. We would associate the relic PWN radiation with the head region, while we attribute the lack of TeV emission in the PWN region to a small number of electrons injected by the "refreshed" PWN. Since the total number of relic electrons injected over a few thousand years is much higher, the head region should produce higher TeV emission via ICS than the PWN. The reported TeV detection in the head region by MAGIC may indicate such ICS emission. The UHE emission in the tail region cannot be caused by relic electrons, which should have cooled quickly to GeV-TeV energies. Instead, particle reacceleration during the SNR-PWN interaction via PWN compression, as proposed by Ohira et al. (2018), may be responsible for producing the UHE emission in the tail. A further study in the entire region, with new VERITAS observation data and more extensive SED study, will be presented in our future paper.

Another key parameter is the proper motion of the pulsar. Although there is yet no direct measurement of the proper motion, the radio and X-ray morphology of the PWN suggest that the pulsar is moving in the northwest direction. It was proposed that the Boomerang-like radio morphology was caused by the PWN colliding with the high-density ISM region

in the northwest boundary of SNR G106.3+2.7. In this scenario, the head is more extended because the relic electrons from the PWN diffuse into a lower-density region. In addition, the X-ray data on torus-jet morphology were fit by a PWN emission model (Ng & Romani 2004) that also supported the proper motion in the northwest direction. Although a future Chandra observation over $\sim\!20\,\mathrm{yr}$ baseline may be able to detect the proper motion, it may be difficult if the source distance is indeed $\sim\!8$ kpc or greater as suggested by our SED and morphology studies presented in this paper.

5. Conclusions

We summarize our findings from our multiwavelength investigation of the Boomerang PWN and its surrounding region.

- (1) We detected a 51.67 ms pulsation with 3–20 keV NuSTAR data and it allowed us to separate the on-pulse component from the PWN emission. With NuSTAR we detected hard X-ray emission from the Boomerang PWN up to 20 keV and found that its size decreases from $r = 33'' \pm 2''$ (3–10 keV) to $20'' \pm 2''$ (10–20 keV).
- (2) Our analysis of the 2002 Chandra data, after excising the pulsar emission, yielded $N_{\rm H}=8.9^{+1.5}_{-1.4}\times10^{21}\,{\rm cm}^{-2}$ and the PWN photon index of $\Gamma=1.52^{+0.13}_{-0.12}$. The hydrogen column density is consistent with the value derived from the pulsar's DM measurement of $(4.3-8.8)\times10^{21}\,{\rm cm}^{-2}$. Joint Chandra and NuSTAR spectral analysis of the PWN measured no X-ray flux variability, and the $0.5-20\,{\rm keV}$ spectra are consistent with a single power-law model with $\Gamma=1.52\pm0.06$.
- (3) Our analysis of the most updated Fermi-LAT and VERITAS data yielded no detection of the Boomerang PWN. We set an upper limit on the gamma-ray flux above 50 GeV of $F \lesssim 10^{-12} \ {\rm erg \ s^{-1} \ cm^{-2}}$.
- (4) Among the previously suggested source distances ranging from 0.8 kpc to \sim 8 kpc (Kothes et al. 2001; Abdo et al. 2009a; He et al. 2013), we found that $d \sim 8$ kpc provides the most plausible solution to fitting the SED data. The widely used source distance of 0.8 kpc leads to radiation efficiencies that are too low and cannot be produced by any of our SED models with reasonable parameters. We note, however, that all SED models used in this paper simplify the complex nature of Boomerang. While the offset between the radio and X-ray peak emission may suggest a multizone system, modeling was done under the assumption that Boomerang is a singlezone system. Implementing a multizone model may boost our understanding of the emission offset between the radio, X-ray, and TeV peak emission. The dynamical SED model used in this paper also assumes that Boomerang is a spherically symmetric PWN, an obvious simplification of the actual morphology. As can be seen in Figure 13, the dynamical SED fits predict strong emission at slightly higher radio frequencies and/or X-ray energies than what has been observed so far. Future analysis of observations in these energy bands could further test the validity of these fits.
- (5) The radiation efficiencies (i.e., $F(4\pi R^2)/\dot{E}$ ratios) of Boomerang are $3 \times 10^{-6} (R/8 \, \text{kpc})^2$, $6 \times 10^{-4} (R/8 \, \text{kpc})^2$, and $4 \times 10^{-4} (R/8 \, \text{kpc})^2$ in the radio, X-ray, and TeV bands, respectively. Assuming a distance of 8 kpc, these

- values are now more consistent with those of other PWNe with similar spin-down powers (Kargaltsev et al. 2013).
- (6) Our SED modeling requires that the current PWN *B*-field should be low $(B \sim 2\text{--}4 \,\mu\text{G})$. Our X-ray PWN size measurements suggest a slightly higher value $(B \sim 6\text{--}14 \,\mu\text{G})$. We ruled out the high *B*-field value $(B = 2.6 \,\text{mG})$ suggested by the radio observations (Kothes et al. 2006), as well as that $(B = 140 \,\mu\text{G})$ suggested by Liang et al. (2022).
- (7) The Boomerang PWN should currently be in its reexpansion phase after having been crushed by the SNR reverse shock. The relic electrons injected earlier before the SNR crush should have produced synchrotron and ICS radiation elsewhere, e.g., in the head region. We attribute the radio break at 4–5 GHz to the minimum energy of the injected electrons. While the origin of this break in the electron spectrum is still unknown, we are confident that the radio break is not caused by synchrotron cooling as was hypothesized by Kothes et al. (2006).
- (8) The origin of the head-tail morphology could be related to the PWN propagating in an inhomogeneous density region and interacting with the SNR, as suggested by hydrodynamic simulations. Following Kothes et al. (2006), we also suspect that the PWN is currently propagating in the northwest direction and expanding in high-density ISM. In order to understand the origin of VHE and UHE gamma rays and their connection to the SNR-PWN system, it would be important to resolve the spatial distribution in the TeV emission in the head and tail regions as well as determine the distance and proper motion of the PSR J2229+6114.

Acknowledgments

Support for this work was provided by NASA through NuSTAR Cycle 6 Guest Observer Program grant NNH19ZDA001N. VERITAS is supported by grants from the U.S. Department of Energy Office of Science, the U.S. National Science Foundation and the Smithsonian Institution, by NSERC in Canada, and by the Helmholtz Association in Germany. This research used resources provided by the Open Science Grid, which is supported by the National Science Foundation and the U.S. Department of Energy's Office of Science, and resources of the National Energy Research Scientific Computing Center (NERSC), a U.S. Department of Energy Office of Science User Facility operated under Contract No. DE-AC02-05CH11231. We acknowledge the excellent work of the technical support staff at the Fred Lawrence Whipple Observatory and at the collaborating institutions in the construction and operation of the instrument.

Facilities: NuSTAR, Chandra, Fermi, VERITAS. Software: HEAsoft (v6.28), NuSTARDAS (v2.0.0), XSPEC (v12.11.1; Arnaud 1996), CIAO (v4.13), Naima (Zabalza 2015), GAMERA (Hahn 2016).

ORCID iDs

I. Pope https://orcid.org/0000-0001-8583-6429
K. Mori https://orcid.org/0000-0002-9709-5389
J. D. Gelfand https://orcid.org/0000-0003-4679-1058
S. P. Reynolds https://orcid.org/0000-0002-5365-5444
S. Safi-Harb https://orcid.org/0000-0001-6189-7665

C. J. Hailey https://orcid.org/0000-0002-3681-145X H. An https://orcid.org/0000-0002-6389-9012 P. Batista https://orcid.org/0000-0001-8138-1391 W. Benbow https://orcid.org/0000-0003-2098-170X M. Capasso https://orcid.org/0000-0002-8136-9461 A. Falcone https://orcid.org/0000-0002-5068-7344 G. M Foote https://orcid.org/0000-0002-2944-6060 W. F Hanlon https://orcid.org/0000-0002-0109-4737 D. Hanna https://orcid.org/0000-0002-8513-5603 O. Hervet https://orcid.org/0000-0003-3878-1677 W. Jin https://orcid.org/0000-0002-1089-1754 P. Kaaret https://orcid.org/0000-0002-3638-0637 D. Kieda https://orcid.org/0000-0003-4785-0101 T. K. Kleiner https://orcid.org/0000-0002-4260-9186 M. J. Lang https://orcid.org/0000-0003-4641-4201 G. Maier https://orcid.org/0000-0001-9868-4700 P. Moriarty https://orcid.org/0000-0002-1499-2667 R. Mukherjee https://orcid.org/0000-0002-3223-0754 S. O'Brien https://orcid.org/0000-0002-9296-2981 R. A. Ong https://orcid.org/0000-0002-4837-5253 N. Park https://orcid.org/0000-0002-4282-736X K. Pfrang https://orcid.org/0000-0002-7990-7179 M. Pohl https://orcid.org/0000-0001-7861-1707 E. Pueschel https://orcid.org/0000-0002-0529-1973 J. Quinn https://orcid.org/0000-0002-4855-2694 K. Ragan https://orcid.org/0000-0002-5351-3323 I. Sadeh https://orcid.org/0000-0003-1387-8915 D. Tak https://orcid.org/0000-0002-9852-2469 D. A. Williams https://orcid.org/0000-0003-2740-9714 J. Woo https://orcid.org/0009-0001-6471-1405

References

Abdelmaguid, M., Gelfand, J., Straal, S., & Gotthelf, E. 2022, X-ray Spectral Analysis and Modeling of the TeV source HESS J1640-465, v1, Zenodo, doi:10.5281/zenodo.6674275 Abdo, A. A., Ackermann, M., Ajello, M., et al. 2009a, ApJ, 706, 1331 Abdo, A. A., Ajello, M., Allafort, A., et al. 2013, ApJS, 208, 17 Abdo, A. A., Allen, B. T., Aune, T., et al. 2009b, ApJL, 700, L127 Abeysekara, A. U., Albert, A., Alfaro, R., et al. 2017, Sci, 358, 911 Abeysekara, A. U., Albert, A., Alfaro, R., et al. 2020, PRL, 124, 021102 Acciari, V. A., Aliu, E., Arlen, T., et al. 2009, ApJL, 703, L6 Acero, F., Ackermann, M., Ajello, M., et al. 2016, ApJS, 223, 26 Albert, A., Alfaro, R., Alvarez, C., et al. 2020, ApJL, 896, L29 Amenomori, M., Bao, Y. W., Bi, X. J., et al. 2021, NatAs, 5, 460 Anders, E., & Grevesse, N. 1989, GeCoA, 53, 197 Arnaud, K. A. 1996, in ASP Conf. Ser. 101, Astronomical Data Analysis Software and Systems V, ed. G. H. Jacoby & J. Barnes (San Francisco, CA: Arons, J. 2012, SSRv, 173, 341 Atwood, W. B., Abdo, A. A., Ackermann, M., et al. 2009, ApJ, 697, 1071 Bachetti, M., Huppenkothen, D., Khan, U., et al. 2022, StingraySoftware/ stingray: Version 1.0, v1.0, Zenodo, doi:10.5281/zenodo.6394742 Bao, Y., & Chen, Y. 2021, ApJ, 919, 32 Bietenholz, M. F., Kronberg, P. P., Hogg, D. E., & Wilson, A. S. 1991, ApJL, 373, L59 Bietenholz, M. F., & Nugent, R. L. 2015, MNRAS, 454, 2416 Breuhaus, M., Hinton, J. A., Joshi, V., Reville, B., & Schoorlemmer, H. 2022, &A, 661, A72 Burgess, D. A., Mori, K., Gelfand, J. D., et al. 2022, ApJ, 930, 148 Cao, Z., Aharonian, F. A., An, Q., et al. 2021, Natur, 594, 33 Cholis, I., Karwal, T., & Kamionkowski, M. 2018, PRD, 98, 063008 Coerver, A., Wilcox, P., Zhang, H., et al. 2019, ApJ, 878, 126 Cordes, J., & Lazio, T. 2002, arXiv:astro-ph/0207156 Cox, P., Kruegel, E., & Mezger, P. G. 1986, A&A, 155, 380 Fang, K., Kerr, M., Blandford, R., Fleischhack, H., & Charles, E. 2022, hRvL, 129, 071101 Ferrand, G., & Safi-Harb, S. 2012, AdSpR, 49, 1313

```
Fujita, Y., Bamba, A., Nobukawa, K. K., & Matsumoto, H. 2021, ApJ,
  912, 133
Gaensler, B. M., & Slane, P. O. 2006, ARA&A, 44, 17
Ge, C., Liu, R.-Y., Niu, S., Chen, Y., & Wang, X.-Y. 2021, Innov, 2, 100118
Gelfand, J. D. 2017, in Radiative Models of Pulsar Wind Nebulae, ed.
   D. F. Torres, Vol. 446 (Berlin: Springer), 161
Gelfand, J. D., Slane, P. O., & Zhang, W. 2009, ApJ, 703, 2051
Giacinti, G., Mitchell, A. M. W., López-Coto, R., et al. 2020, A&A, 636, A113
Hahn, J. 2016, ICRC (The Hague), 34, 917
Halpern, J. P., Camilo, F., Gotthelf, E. V., et al. 2001a, ApJL, 552, L125
Halpern, J. P., Gotthelf, E. V., Camilo, F., Collins, B., & Helfand, D. J. 2002,
   in ASP Conf. Ser. 271, Neutron Stars in Supernova Remnants, ed.
   P. O. Slane & B. M. Gaensler (San Francisco, CA: ASP), 199
Halpern, J. P., Gotthelf, E. V., Leighly, K. M., & Helfand, D. J. 2001b, ApJ,
   547, 323
Harrison, F. A., Craig, W. W., Christensen, F. E., et al. 2013, ApJ, 770, 103
Hartman, R. C., Bertsch, D. L., Bloom, S. D., et al. 1999, ApJS, 123, 79
Hattori, S., Straal, S. M., Zhang, E., et al. 2020, ApJ, 904, 32
He, C., Ng, C. Y., & Kaspi, V. M. 2013, ApJ, 768, 64
Joncas, G., & Higgs, L. A. 1990, A&AS, 82, 113
Kargaltsev, O., Rangelov, B., & Pavlov, G. G. 2013, arXiv:1305.2552
Kolb, C., Blondin, J., Slane, P., & Temim, T. 2017, ApJ, 844, 1
Kothes, R., Landecker, T. L., & Wolleben, M. 2004, ApJ, 607, 855
Kothes, R., Reich, W., & Uyanıker, B. 2006, ApJ, 638, 225
Kothes, R., Uyaniker, B., & Pineault, S. 2001, ApJ, 560, 236
Kuiper, L., & Hermsen, W. 2015, MNRAS, 449, 3827
Lang, C. C., Wang, Q. D., Lu, F., & Clubb, K. I. 2010, ApJ, 709, 1125
Liang, X.-H., Li, C.-M., Wu, Q.-Z., Pan, J.-S., & Liu, R.-Y. 2022, Univ, 8, 547
Liu, Q.-C., Zhou, P., & Chen, Y. 2022, ApJ, 926, 124
```

```
López-Coto, R., de Oña Wilhelmi, E., Aharonian, F., Amato, E., & Hinton, J.
  2022, NatAs, 6, 199
MAGIC Collaboration, Abe, H., Abe, S., et al. 2023, A&A, 671, A12
Martin, J., Torres, D. F., Cillis, A., & de Oña Wilhelmi, E. 2014, MNRAS,
  443, 138
Ng, C. Y., & Romani, R. W. 2004, ApJ, 601, 479
Nynka, M., Hailey, C. J., Reynolds, S. P., et al. 2014, ApJ, 789, 72
Ohira, Y., Kisaka, S., & Yamazaki, R. 2018, MNRAS, 478, 926
Oka, T., Saito, T., Kubo, H., & Strzys, M. 2021, ICRC (Berlin), 37, 796,
  https://pos.sissa.it/395/796/pdf
Park, N. & VERITAS Collaboration 2015, ICRC (The Hague), 34, 771
Perkins, J. S., Maier, G. & The VERITAS Collaboration 2009,
  arXiv:0912.3841
Pineault, S., & Joncas, G. 2000, AJ, 120, 3218
Reynolds, S. P., Borkowski, K. J., & Gwynne, P. H. 2018, ApJ, 856, 133
Straal, S. M., Gelfand, J. D., & Eagle, J. L. 2023, ApJ, 942, 103
Strong, A. W., Moskalenko, I. V., & Reimer, O. 2000, ApJ, 537, 763
Taylor, J. H., & Cordes, J. M. 1993, ApJ, 411, 674
Temim, T., Slane, P., Castro, D., et al. 2013, ApJ, 768, 61
Temim, T., Slane, P., Kolb, C., et al. 2015, ApJ, 808, 100
Torres, D. F., Martín, J., de Oña Wilhelmi, E., & Cillis, A. 2013, MNRAS,
  436, 3112
Wik, D. R., Hornstrup, A., Molendi, S., et al. 2014, ApJ, 792, 48
Wilms, J., Allen, A., & McCray, R. 2000, ApJ, 542, 914
Wood, M., Caputo, R., Charles, E., et al. 2017, ICRC (Busan), 301, 824
Xin, Y., Zeng, H., Liu, S., Fan, Y., & Wei, D. 2019, ApJ, 885, 162
Yao, J. M., Manchester, R. N., & Wang, N. 2017, ApJ, 835, 29
Zabalza, V. 2015, ICRC (The Hague), 34, 922
```